The Astrophysical Journal, 974:143 (24pp), 2024 October 10 https://doi.org/10.3847/1538-4357/ad6b28

Bayesian Black Hole Photogrammetry

Dominic O. Chang[1,2], Michael D. Johnson[2,3], Paul Tiede[2,3], and Daniel C. M. Palumbo[2,3]
[1] Department of Physics, Harvard University, Cambridge, Massachusetts 02138, USA; dochang@g.harvard.edu
[2] Black Hole Initiative at Harvard University, 20 Garden Street, Cambridge, MA 02138, USA
[3] Center for Astrophysics | Harvard & Smithsonian, 60 Garden Street, Cambridge, MA 02138, USA
Received 2024 May 3; revised 2024 July 5; accepted 2024 July 12; published 2024 October 9

Abstract

We propose an analytic dual-cone accretion model for horizon-scale images of the cores of low-luminosity active galactic nuclei, including those observed by the Event Horizon Telescope (EHT). Our model is of synchrotron emission from an axisymmetric, magnetized plasma, constrained to flow within two oppositely oriented cones that are aligned with the black hole's spin axis. We show this model can accurately reproduce images of a variety of time-averaged general relativistic magnetohydrodynamic simulations and that it accurately recovers the black hole spin, orientation, emission scale height, peak emission radius, and fluid flow direction from these simulations within a Bayesian inference framework using radio interferometric data. We show that nontrivial topologies in the images of relativistic accretion flows around black holes can result in nontrivial multimodal solutions when applied to observations with a sparse array, such as the EHT 2017 observations of M87*. The presence of these degeneracies underscores the importance of employing Bayesian techniques to adequately sample the posterior space for the interpretation of EHT measurements. We fit our model to the EHT observations of M87* and find a 95% highest posterior density interval for the mass-to-distance ratio of $\theta_g \in (2.84,\ 3.75)\ \mu$as, and give an inclination of $\theta_o \in (11°, 24°)$. These new measurements are consistent with mass measurements from the EHT and stellar dynamical estimates and with the spin axis inclination inferred from properties of the M87* jet.

Unified Astronomy Thesaurus concepts: Supermassive black holes (1663)

1. Introduction

In 2017, the Event Horizon Telescope Collaboration (EHTC) observed the supermassive black hole, M87*, at the center of the elliptical galaxy, Messier 87 using a seven-element Very Long Baseline Interferometry (VLBI) array operating at $\lambda = 1.3$ mm. The resulting Event Horizon Telescope (EHT) images of M87* revealed a dark central brightness depression, consistent with expectations for accretion flows within a Kerr spacetime (EHTC et al. 2019a, 2019b, 2019c, 2019d, 2019e, 2019f, 2021a, 2021b, 2023, hereafter M87* I–IX). More recently, the EHTC has also published images of the supermassive black hole Sgr A* at the center of the Milky Way (EHTC et al. 2022a, 2022b, 2022c, 2022d, 2022e, 2022f, 2024a, 2024b, hereafter Sgr A* I–VIII). These images now provide the most direct evidence for the existence of supermassive black holes.

A crucial question is what insights into the properties of both supermassive black holes and their immediate environments are possible through the EHT measurements and the resulting images, a question that falls under the broader science of photogrammetry. For instance, the 2017 campaign allowed the EHTC to constrain the diameter of the bright emission ring in M87* to be $d = 42 \pm 3\ \mu$as. However, mass measurements from the diameter of the emission ring on an image (often called the diameter of the "apparent shadow") are dependent on assumptions about the emission geometry (see, for example, M87* V, M87* VI; and Gralla et al. 2019). To relate the measured diameter of the emission ring to the black hole mass-to-distance ratio (or angular gravitational radius), $\theta_g \equiv GM/(c^2D)$, the EHTC introduced an unknown scaling factor, α (M87* VI):

$$d = \alpha\ \theta_g. \tag{1}$$

The EHTC estimated α and its associated uncertainty using a suite of general relativistic magnetohydrodynamic (GRMHD) simulations (M87* V). These ab initio simulations self-consistently evolve a magnetized fluid in the Kerr spacetime and have been successful in producing a broad range of phenomena seen in LLAGN, from horizon-scale image structures and variability seen with the EHT to powerful, large-scale jets with multiwavelength emission. This approach resulted in a reported mass measurement for M87* of $M = 6.5 \pm 0.2|_{\rm stat} \pm 0.7|_{\rm sys} \times 10^9 M_\odot$ (M87* VI). In this estimate, the dominant uncertainty corresponds to that of α (i.e., systematic uncertainty associated with the unknown emission properties and spin).

Apart from the EHTC's mass measurement, there is a rich literature of other methods to infer the mass of M87* from observations on much larger length scales. These methods model the resolved emission spectra of the region surrounding M87* with different components of origin, usually either from the dynamics of gas in the circumnuclear disk around M87* (see, for example, macchetto et al. 1997; Walsh et al. 2013) or from the stellar velocity dispersion in the bulge (σ_*; see Gebhardt et al. 2011; Liepold et al. 2023; Simon et al. 2023). There has historically been a discrepancy in the measured mass, both between and within these two methodologies. The gas dynamical mass measurements are typically only $\sim$ half the value of the smallest stellar dynamics measurements. Moreover, different modeling choices may result in large systematic uncertainties (see, e.g., Jeter & Broderick 2021; Simon et al. 2023).

The EHTC results thus provide a crucial input to assess these alternative mass measurements, but the α-calibration approach may also have unknown systematic errors and is dependent on the selection of GRMHD models (M87* V). More recent analyses using semianalytic models have found that this type of calibration can provide estimates for the mass-to-distance ratio with ∼10% systematic uncertainty (Özel et al. 2022; EHTC et al. 2022f; Younsi et al. 2023a). Nevertheless, even for GRMHD simulations, some models in the EHTC library that are consistent with the 2017 EHT observations would give significantly different mass inferences but were excluded based on additional constraints on the observed jet power and X-ray luminosity of M87* (M87* V). Hence, other approaches to black hole parameter inference from EHT data are of significant value in substantiating these conclusions and could provide sharper estimates of the black hole properties.

Palumbo et al. (2022) provided one such alternative: a mass inference scheme that involves fitting EHT data using a model whose parameters are described by both the black hole spacetime and a flexible emission geometry. The emission model was taken to be purely equatorial and optically thin. Using time-averaged GRMHD simulations, the authors show that this approach gives accurate mass measurements for magnetically arrested disk (MAD; Narayan et al. 2003) simulations, albeit with a modest (∼10%) underestimate in some simulations. However, the approach gives poorer mass estimates for standard and normal evolution (SANE; Narayan et al. 2012) simulations. Although the authors did not infer a mass from the true EHT data, which favor MAD models, their work shows the potential for using simple emission models to derive information about a black hole mass and emission geometry from EHT data.

In this paper, we develop a simple, flexible model for images of accretion flows around supermassive black holes. We show that the model is capable of not only inferring spacetime parameters but also measuring the 3D structure of the inner emission geometry—effectively enabling photogrammetry within a curved spacetime. Our model extends the equatorial version defined in Palumbo et al. (2022) to a biconical region aligned with the spin axis, motivated by optically thin emitting material concentrated within a jet sheath or accretion disk near a Kerr black hole as seen in a variety of numerical simulations (e.g., Dexter et al. 2012; Mościbrodzka et al. 2016; EHTC et al. 2019f; Wong et al. 2021). The primary advantage of our model relative to more sophisticated physical approaches is that it is analytic and differentiable. These features allow the model to be suitable for performing Bayesian inference of black hole spacetime and emission parameters directly from interferometric measurements, such as those of the EHT. In addition, the model captures the salient features in GRMHD images for both MAD and SANE simulations and allows a crisp exploration of degeneracies in images that can arise between the parameters of the black hole and those of the synchrotron-emitting plasma.

The paper is outlined as follows. In Section 2, we introduce our emission model and describe how it is used to produce images. In Section 3, we assess the ability of this model to reproduce the images seen in a variety of GRMHD simulations. In Section 4, we use this model to fit EHT observations of M87*. In Section 5, we summarize our results.[4]

[4] A repository of scripts used in this analysis are open source and are available for download (Chang 2024).

2. Description of the Model

2.1. Motivations and Assumptions

The standard anatomy of active galactic nuclei (AGN) is of a rotating supermassive black hole accreting a disk of magnetized plasma. AGN are often associated with collimated relativistic jets with observed spectra ranging from radio to X-ray (see Blandford et al. 2019, for a review on AGN jets). The bolometric luminosities of AGN are typically low when compared to the Eddington luminosity, $L_{\rm Edd} = 4\pi GMc/\kappa_{\rm es}$, where $\kappa_{\rm es}$ is the electron scattering cross section, which can be related to the accretion rate through $L_{\rm Edd} = 0.1\dot{M}_{\rm Edd}c^2$ (Yuan & Narayan 2014). Low-luminosity AGN (LLAGN) feature luminosities substantially below $L_{\rm Edd}$. For instance, M87* and Sgr A* are estimated to have luminosities of $3.6 \times 10^{-6} L_{\rm Edd}$ and $2 \times 10^{-9} L_{\rm Edd}$, respectively (Prieto et al. 2016; EHTC et al. 2022e), implying that these systems are greatly underfed.

LLAGN are thus thought to be well described by hot accretion flows that are radiatively inefficient. These flows often rise to relativistic jets and feature characteristically geometrically thick accretion disks that are optically thin at radio wavelengths (Yuan & Narayan 2014). Many authors have previously used simple geometric models that feature these assumptions to describe the inner accretion flow around supermassive black holes. These efforts include a series of works that developed semianalytic models of a radiatively inefficient accretion flow (Broderick et al. 2009, 2011, 2014, 2016; Pu et al. 2016; Pu & Broderick 2018; Broderick et al. 2020) and of emission from jets (e.g., Broderick & Loeb 2009), which report constraints on the spin, inclination, and position angle (p.a.) of M87* and Sgr A*.

These simple models complement the more complex GRMHD simulations that are the basis for most theoretical interpretations of the EHTC. Both types of models have been used to show that some image features, such as the black hole's apparent shadow, are largely independent of the underlying accretion physics when observed at millimeter wavelengths (for example, the conservative fluid models of Özel et al. 2022; Younsi et al. 2023; Papoutsis et al. 2023; and general relativistic particle in cell models of Galishnikova et al. 2023 yield similar results). GRMHD simulations have the additional benefit of self-consistently modeling source variability. The 2017 observations of Sgr A* by the EHT, however, imply that the observed variability is in tension with the predictions of GRMHD (see, e.g., Sgr A* IV).

In creating this model, we are guided by the time-averaged emission structure observed from GRMHD simulations. This approach allows us to efficiently achieve physically relevant image structures from physically motivated parameters, without the long computational times required to realize them in GRMHD simulations.

With the previously discussed considerations in mind, we take the following features as guiding assumptions for the design of our model:

1. The emission is synchrotron radiation from a magnetized plasma.
2. The accretion flow is relatively optically thin to millimeter wavelengths (Falcke et al. 1998; Duschl 1999).
3. The emission region is compact and lies within a few gravitational radii of the black hole, with the bulk millimeter wavelength emission often being produced in

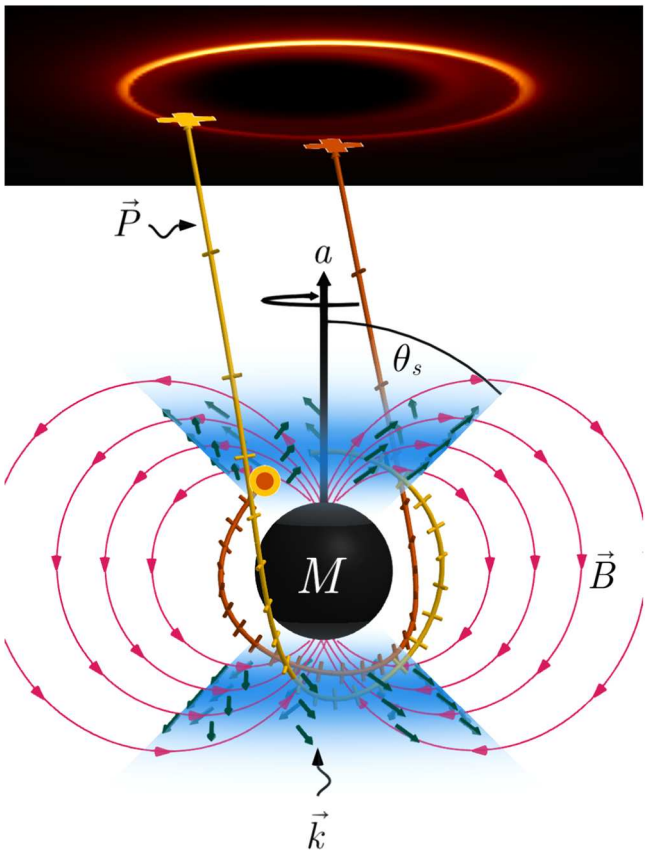

Figure 1. Schematic depiction of our dual-cone emission model. The full model consists of a Kerr black hole (black sphere) surrounded by synchrotron-emitting plasma (green arrows) confined to a cone of opening angle θ_s and threaded by a magnetic field $\boldsymbol{B}$ (red field lines). The magnetic field and plasma are taken to be axisymmetric about the equatorial plane. The emission is concentrated at a characteristic radius, R, with the profile determined by a double power-law distribution with exponents p_1 and p_2 (translucent blue cone). The polarization from the synchrotron radiation is parallel transported along null-geodesics (yellow and orange ticked trajectories) to generate an image on the screen of an observer at radial infinity. The image generated from the model is the sum of multiple subimages corresponding to the different trajectories light can take from the source to the observer.

regions along the jet sheath and near the jet base (Dexter et al. 2012; Emami et al. 2023).

4. The flow is taken to be axisymmetric since it should reflect the time-averaged structure of the accretion flow.
5. The emission is restricted to lie on two oppositely oriented conical surfaces that are centered about the spin axis of the black hole.

The last assumption is motivated from observed locations of the peak mean emission within GRMHD simulations, which are seen to typically lie in the jet/disk boundary region. GRMHD simulations, with thermal electron distribution functions in particular, are seen to span a wide range of peak emission opening angles (see for example Figures 3 and 4 of Emami et al. 2023) that range from either being flushed to the equatorial plane, a characteristic of low $R_{\rm high}$ MAD simulations, or significantly off the equatorial plane, as observed in high $R_{\rm high}$ SANE simulations (M87* V).

2.2. The Emission Model

Figure 1 is a schematic of the emission model. Our model can be described as a compact, axisymmetric, linearly polarized emissivity that is constrained to lie on a dual-cone with opening angle θ_s. The emissivity is determined by the interactions of a magnetic field with a plasma flow around the black hole. The plasma flow is constrained to move along the surface of the cone, while the magnetic field can orient freely.

Following Palumbo et al. (2022), we impose a compactness constraint on the emission by choosing a radially dependent, double power-law profile on the emissivity given by

$$\mathcal{J}(r, R, p_1, p_2) = \frac{(r/R)^{p_1}}{1 + (r/R)^{p_1+p_2}}, \tag{2}$$

where r is the emission radius, R is the characteristic radius of the profile, p_1 is the exponent of the inner power law, and p_2 is the exponent of the outer power law. When given a magnetic field, B, and plasma fluid velocity, u, we can write our spectral intensity function as

$$I_\nu(r, R, p_1, p_2, B, u) \propto \mathcal{J}(r, R, p_1, p_2) P_\nu(B, u), \tag{3}$$

where P_ν is the linear polarization intensity of synchrotron emission (we provide a simple power-law prescription for P_ν below). We ignore the missing proportionality constant and electron number density dependencies for this study since our analyses in Sections 3 and 4 are independent of the overall flux of the image.

As with the emission models of Gelles et al. (2021), Narayan et al. (2021), and Palumbo et al. (2022), the calculation of P_ν is reliant on transformations to the frames of the asymptotic observer (Boyer–Lindquist frame), a zero angular momentum observer (ZAMO), and the fluid frame. Although our construction of these frames is qualitatively similar to that of Narayan et al. (2021) and Gelles et al. (2021), we will summarize the procedure here since some differences are introduced by the nonequatorial emission geometry.

The Kerr line element in Boyer–Lindquist coordinates is given by (Chandrasekhar 1984)

$$ds^2 = -\frac{\Delta\Sigma}{\Xi}dt^2 + \frac{\Sigma}{\Delta}dr^2 + \Sigma d\theta^2 + \frac{\Xi \sin^2\theta}{\Sigma}[d\phi - \omega dt]^2, \tag{4}$$

where

$$\Delta(r) = r^2 - 2Mr + a^2, \quad \Sigma(r, \theta) = r^2 + a^2\cos^2\theta,$$
$$\omega = \frac{2aMr}{\Xi}, \quad \Xi = (r^2 + a^2)^2 - \Delta a^2 \sin^2\theta. \tag{5}$$

The transformation for covector components from the global Boyer–Lindquist frame to the local ZAMO frame is then described by the tetrad, $e^\mu_{(m)}$, where we have used Greek indices to label components with respect to the global Boyer–Lindquist basis, and parenthesized Latin indices to label components with respect to the local ZAMO basis. The components of the tetrads are (Bardeen et al. 1972)[5]

$$e_{(0)} = \sqrt{\frac{\Xi_s}{\Sigma_s\Delta_s}}(\partial_t + \omega_s\partial_\phi), \tag{6a}$$

[5] Our definition of the tetrad basis ordering matches the definitions in Gelles et al. (2021), Narayan et al. (2021), and Palumbo et al. (2022), but not the traditional basis ordering. The negation of $e^{(3)}$ from its traditional definition ensures that the basis is always right-handed.

$$e_{(1)} = \sqrt{\frac{\Delta_s}{\Sigma_s}}\,\partial_r, \tag{6b}$$

$$e_{(2)} = \sqrt{\frac{\Sigma_s}{\Xi_s}}\,\frac{1}{\sin\theta_s}\partial_\phi, \tag{6c}$$

$$e_{(3)} = -\frac{1}{\sqrt{\Sigma_s}}\partial_\theta, \tag{6d}$$

where Ξ_s, ω_s, Σ_s, and Δ_s are the values of Ξ, ω, Σ, and Δ evaluated at the emission radius, r_s and emission inclination, θ_s. The ZAMO frame is labeled with directions $\{\hat{x}^0, \hat{x}^1, \hat{x}^2, \hat{x}^3\}$, which form a nonholonomic basis. This choice of ZAMO basis orientation ensures that $\hat{x}^1$ and $\hat{x}^2$ lie in the tangent space of the emission cone.

The fluid frame is defined from the fluid velocity vector,

$$u^{(m)} = \beta_v \langle 0, \cos\chi, \sin\chi, 0\rangle^{(m)}, \tag{7}$$

which depends on an azimuthal angle χ, that winds from the $\hat{x}^{(1)}$ direction to the $\hat{x}^{(2)}$ direction, and fluid speed β_v. Since $\hat{x}^{(2)} || \hat{\phi}$, then we take the following cases to define whether the fluid is in prograde or retrograde motion with respect to the hole:

$$\begin{cases} \text{sign}(\chi) = \text{sign}(a) & \text{Prograde} \\ \text{sign}(\chi) \neq \text{sign}(a) & \text{Retrograde.} \end{cases} \tag{8}$$

Both, χ and β_v are measured in the frame of the ZAMO. Our definition of the fluid velocity vector constrains it to lie in the tangent space of the dual-cone. The fluid velocity vector can be used to construct a fluid frame through Lorentz transformation from the ZAMO frame,

$$f^{(m')} = \Lambda^{(m')}{}_{(n)} f^{(n)}, \tag{9}$$

where we have used the parenthesized primed Latin indices to label the fluid frame components.

We assume that the polarization intensity scales as a power law,

$$P \propto \delta^{3+\sigma} l_p |\boldsymbol{B}|^{1+\sigma} \sin^{1+\sigma}\zeta. \tag{10}$$

This precise relationship can arise from power-law distributions for the electron number densities and energies, but it is approximately true under much more general cases (Narayan et al. 2021). The resulting polarization intensity is then determined by a spectral index (σ), Doppler factor (δ; which includes gravitational redshift and velocity effects), and the magnetic field in the fluid frame ($B^{(m')}$). The remaining quantities are l_p, which is a proxy for the path length through a cone of width H that depends on the emitting photon four momentum $p^{(m')}$ as

$$l_p = \frac{p^{(0')}}{p^{(3')}} H, \tag{11}$$

and ζ, the angle associated with the cross product of $p^{(m')}$ and $B^{(m')}$ in the fluid frame,

$$\sin\zeta = \frac{|\boldsymbol{p} \times \boldsymbol{B}|}{|\boldsymbol{p}||\boldsymbol{B}|}. \tag{12}$$

Here, the vector quantities $\boldsymbol{p}$ and $\boldsymbol{B}$ are the purely space-like components of $p^{(m')}$ and $B^{(m')}$.

We parameterized the direction of $B^{(m')}$ in terms of the fluid frame polar angle, ι, and the fluid frame azimuthal angle η as

$$B^{(m')} \propto \langle 0, \sin(\iota)\cos(\eta), \sin(\iota)\sin(\eta), \cos(\iota)\rangle^{(m')}. \tag{13}$$

The polarization direction is taken to be orthogonal to the magnetic field at the point of emission. We will require that the radial and azimuthal components of the magnetic field in each cone have opposite signs as a proxy for the lines being dragged by the plasma flow or black hole, and to ensure that the global magnetic field remains divergence free. That is, for a given η and ι, then the magnetic fields can be written as[6]

$$\boldsymbol{B}|_{\text{cone}_1}(\iota, \eta) = \boldsymbol{B}|_{\text{cone}_2}(-\iota, \eta). \tag{14}$$

The polarized emission is then raytraced, and parallel transported to a distant observer through conservation of the Walker–Penrose constant (Walker & Penrose 1970; Chandrasekhar 1984),

$$\kappa = (A - iB)(r - ia\cos\theta) \equiv \kappa_1 + i\kappa_2, \tag{15}$$

where

$$A = (P^r p^t - p^r P^t) + a\sin^2\theta_s (P^\phi p^r - p^\phi P^r), \text{ and} \tag{16}$$

$$B = [(r^2 + a^2)(p^\phi P^\theta - p^\theta P^\phi) - a(p^t P^\theta - p^\theta P^t)]\sin\theta, \tag{17}$$

$p^\mu = (p^t, p^r, p^\theta, p^\phi)$ is the photon momentum in Boyer–Lindquist coordinates, and $P^\mu = (P^t, P^r, P^\theta, P^\phi)$ is the polarization vector. Although our model naturally produces images with polarized emission structure, the rest of this work will be focused on studies of the total intensity.

2.2.1. Raytracing

The construction of our model allows us to produce images using analytic solutions of the Kerr geodesic equations. This fact makes the evaluation of our model extremely efficient, a necessary condition for performing posterior explorations of fits to realistic data, which will be discussed in Section 4. Our raytracing procedure is similar to that of Gelles et al. (2021), with the exception that the presence of nonequatorial emitters requires (i) the inclusion of vortical trajectories to the geodesic solution space, and (ii) a new definition of subimage indexing that is different from ones used by previous authors (e.g., Bao et al. 1994; Johnson et al. 2020; Wong et al. 2022). We will briefly outline how we use the solutions to the geodesic equations to raytrace our model; Appendix A.3 provides details on our image indexing definition.

The solutions to the geodesic equations can be found by a reduction to quadratures through the Hamilton–Jacobi approach (Carter 1968; Dexter & Agol 2009; Gralla & Lupsasca 2020; Himwich et al. 2020). The four-momenta, $p_\mu = g_{\mu\nu}\frac{dx^\mu}{d\tau'}$, of the photons for an affine parameter τ' are then written as

$$p_\mu dx^\mu = -dt \pm_r \frac{\sqrt{\mathcal{R}(r)}}{\Delta(r)} dr \pm_\theta \sqrt{\Theta(\theta)}\, d\theta + \lambda d\phi, \tag{18}$$

where $\pm_r$ and $\pm_\theta$ are chosen appropriately for photons that are outgoing/ingoing and inclining/declining. The other terms in

[6] We have relaxed the assumption of Narayan et al. (2021) and Palumbo et al. (2022) that relates η and χ, and have chosen instead to make them independent.

Equation (18) are the radial potential of the photon given by

$$\mathcal{R}(r) = (r^2 + a^2 - a\lambda)^2 - \Delta[\eta + (a - \lambda)^2], \quad (19)$$

the θ-potential,

$$\Theta(\theta) = \eta + a^2 \cos^2\theta - \lambda^2 \cot^2\theta, \quad (20)$$

the energy reduced azimuthal momentum, λ, and the energy reduced Carter integral, η.

When expressed in this form, it is typical to parameterize the solutions to the geodesic equations in terms of the Mino time, τ (Mino 2003):

$$\Sigma(r, \theta) d\tau = d\tau'. \quad (21)$$

The Mino time can then be expressed as integrals in terms of either r or θ, which both have solutions in terms of elliptic integrals (for a review of the solutions to the Kerr geodesic equations, see Rauch & Blandford 1994; Gralla & Lupsasca 2020):

$$\Delta\tau = \int_{r_s}^{r_o} \frac{dr}{\sqrt{\mathcal{R}(r)}} = \int_{\theta_s}^{\theta_o} \frac{d\theta}{\sqrt{\Theta(\theta)}}. \quad (22)$$

The elliptic integrals can be inverted to allow their amplitudes to be expressed in terms of Jacobi elliptic functions. It is therefore possible to write expressions that relate the emission radius of a null-geodesic in terms of emission inclination, θ_s, observation inclination, θ_o, observer screen coordinates, (α, β), and the order of subimage, n,

$$r_s = r(\theta_s, \theta_o, \alpha, \beta, n), \quad (23)$$

without the need for a numerical raytracing algorithm to solve the second order geodesic equations (e.g., Mościbrodzka et al. 2016; Bronzwaer et al. 2018). We use Equation (3) with Equation (23) to calculate the intensity received at pixel with coordinates α, β as

$$\mathcal{I}_\nu(\alpha, \beta) \propto \sum_{\theta_s} \sum_{n} I_\nu(r_s(\theta_s, \theta_o, \alpha, \beta, n), R, p_1, p_2). \quad (24)$$

3. Image-domain Comparisons with GRMHD

We test the feasibility of using the dual-cone model to represent the horizon-scale structure of LLAGN cores by studying its ability to reproduce images of time-averaged GRMHD models of Sgr A* and M87*. These include GRMHD simulations of MAD and SANE (standard and normal) accretion flows, which are described by the strength of their magnetic flux across the midplane. MAD models typically feature high magnetic pressure, with ordered field lines, and greater jet power, while SANE models feature higher fluid pressure and more turbulent flows. The MAD accretion flows are of particular interest since they exhibit more jet power than their SANE counterparts, and are largely more consistent with EHT data (see analyses of M87* VI, Sgr A* V). For our study, we use time-averaged `iHARM` and `KHARMA` GRMHD models of MAD and SANE accretion flows from the Illinois simulation library (EHTC et al. 2019f; Prather et al. 2021; EHTC et al. 2022e), whose emissivities are extracted and imaged with the `ipole` general relativistic radiative transfer code in the `PATOKA` pipeline (Mościbrodzka & Gammie 2018; Wong et al. 2022). The emission from these models is dependent on a simple prescription for the ion-to-electron temperature ratio of the fluid:

$$\frac{T_i}{T_e} = \mathrm{R_{high}} \frac{\beta_p^2}{1 + \beta_p^2} + R_{\mathrm{low}} \frac{1}{1 + \beta_p^2}, \quad (25)$$

where $\beta_p = P_{\mathrm{gas}}/P_{\mathrm{mag}}$ gives the ratio of the gas-to-magnetic pressure. The two tuning parameters R_{high} and R_{low} tend to describe the temperature ratios in the (weakly magnetized) disk and the (strongly magnetized) jet, respectively.

The analyses in this section were performed using a template matching algorithm implemented in `VIDA.jl` (Tiede et al. 2022) to generate image-domain representations of GRMHD from a set of three different model classes. Our analysis requires the definition of a loss function between images, which we take to be the log of the magnitude of the normalized cross correlation (NxCorr) between two $N \times N$ images. The NxCorr between two images A and B is given by

$$\mathrm{NxCorr} = \left| \frac{\sum_i (A_i - \mu_A)(B_i - \mu_B)}{\sqrt{\sum_i (A_i - \mu_A)^2} \sqrt{\sum_j (B_i - \mu_B)^2}} \right|, \quad (26)$$

where μ_A and μ_B are the average intensity of the two images, and $i, j \in \{1,\ldots,N\}$ labels their pixels. We use `BlackBoxOptim.jl`, a `julia` implementation of a differential evolution algorithm, to minimize the loss function between images of our model and GRMHD. We will refer to the models that generate the best-fit images as "representative models," which we will use to perform photogrammetry on the images of the GRMHD simulation and infer its 3D emission structure.

3.1. Image-domain Fit: Simulations of M87*

We compare the performance of three different classes of analytic models with different emission geometries. These are (i) an equatorial model, similar to the one described in Palumbo et al. (2022), (ii) our dual-cone model described in Section 2, and (iii) a "combination" model whose emission is the sum of the two. These models are used to generate images that are similar to those produced by time averaging an $a = 0.94$, prograde, $R_{\mathrm{high}} = 10$, MAD GRMHD simulation and an $a = 0.94$ spin, prograde, $R_{\mathrm{high}} = 160$, SANE simulation. Both simulations are taken to have mass-to-distance ratios of 3.83 μas, matching EHT measurements of M87* (M87* V). An equivalent fit to an $a = 0.5$ $R_{\mathrm{high}} = 20$ MAD and an $a = 0.5$ $R_{\mathrm{high}} = 160$ SANE is shown in Figure 15 in Appendix B. The parameter search range used to find the representative images of our models is detailed in Table 4.

Figure 2 shows a summary of images of our representative models. These are all compared to the GRMHD model they were fitted to in the first row. The general effect of R_{high} is to tune the relative emission contribution from the jet and the disk. Although trends with respect to R_{high} differ in MADs and SANEs, due to their different magnetic field strengths in the inner accretion flow (compare, for example, the emissivities between models in EHTC et al. 2019f; Emami et al. 2023), the simulations in the top row of Figure 2 are typical of the extreme cases of emission scale heights seen in GRMHD. In particular, low R_{high} MAD simulations tend to have emission geometries with lower scale heights (more disk dominated), and high R_{high}

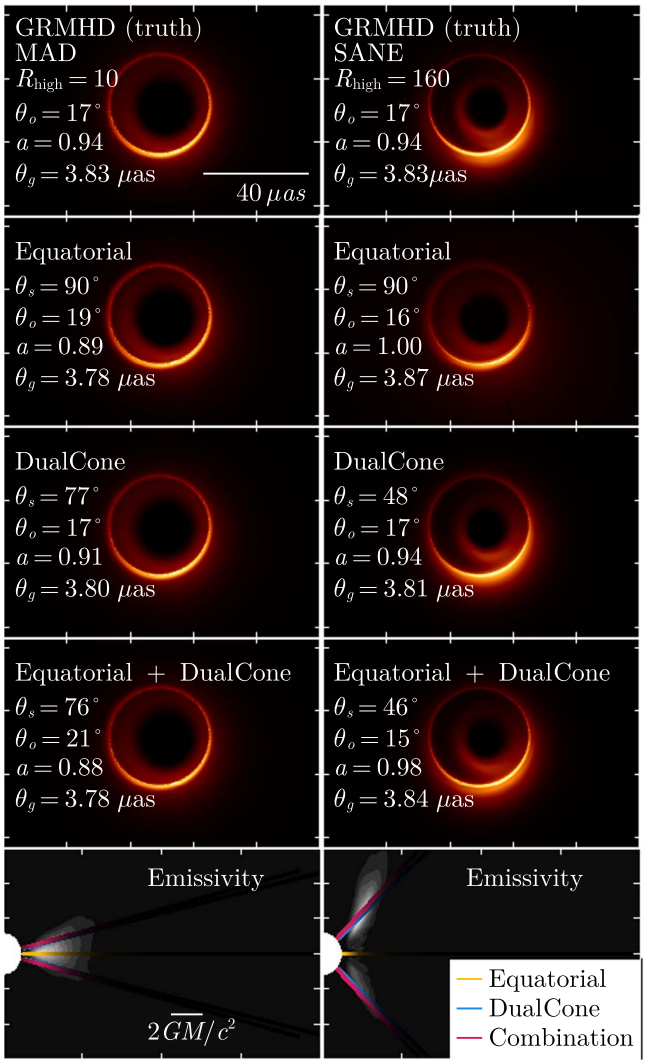

Figure 2. Comparison of time-averaged MAD (left) and SANE (right) GRMHD simulations of M87* (top row) with the best-fitting equatorial (second row), dual-cone (third row), and combination (equatorial + dual-cone) models (fourth row). These two simulations are representative of the minimal and maximal emission scale heights that are typically seen in GRMHD simulations of M87*. The best-fitting models are determined by maximizing the normalized cross correlation in the image domain. The text in each panel gives the opening angle of the cone (θ_s), the viewing inclination (θ_o), the black hole spin (a), and the mass-to-distance ratio (θ_g). The bottom row compares the fitted emissivity functions of our models (colored lines) to the true emissivity of the GRMHD (grayscale). The predicted emissivities are consistent with those of the GRMHD, as is evident by their overlap, which illustrates our model's ability to perform photogrammetry in black hole spacetimes.

SANE simulations tend to have emission geometries with high scale heights (more jet dominated).

The increased emission contribution from the forward jet in the images of the SANE model of Figure 2 manifests as a smaller secondary ring feature. The morphology of this feature is difficult for simple equatorial models to produce, as is evident when comparing the true images to the images of the equatorial model (second row in Figure 2) to the true images of the GRMHD. The existence of such features is, however, captured by models capable of producing jetlike emission, as is apparent in the images of the geometric models with off-equatorial components (the dual-cone and combination models of the third and fourth rows).

Of interest are the inferred bulk parameters of the accretion flow and spacetime from our models. We note, for example, that the fitted mass-to-distance ratio, spin, and observer inclinations of all our models are correct to within 3%, 5%, and 10%, respectively. The left and right panels in the last row of Figure 2 show the emission geometries of each of the representative models overlayed on the true emissivity contours of the MAD and SANE GRMHD simulations, respectively. All representative models capture the compactness of the peak emission, but only the dual-cone and combination models are able to capture the scale height of the true emission geometries. Thus, the dual-cone models appear capable of performing accurate photogrammetry of the emission geometry from images of GRMHD.

3.2. *Image-domain Fit: Simulations of Sgr A**

In models of M87*, such as those in Figure 2, the low observer inclination allows for 2D emissivities to adequately represent the screen projection of the 3D structures seen in GRMHD. Images of simulations viewed at higher inclinations, in contrast, may be more sensitive to edge-on effects that are not captured by our model. We evaluate the performance of our models at fitting images taken at varying observer inclinations by fitting images of $R_{\rm high} = 160$ GRMHD simulations of Sgr A* from the Illinois simulation registry. These simulations were raytraced to produce images at inclinations of 30°, 50°, 70°, and 90° (see Figure 3).

All models are again able to recover the true θ_g values of the source within good accuracy, fitting values within 1% of the truth, but tend to have a bias toward inferring lower masses as the tilt of the source increases. The models tend to be less accurate on spin inferences at high inclinations but perform well at low and moderate inclinations of 30°, 50°, and 70°, capturing the true spin to within 5%. The decreased accuracy of our model at recovering the true black hole parameters at moderate and high inclinations is likely a result of it providing worse image representations of structures seen at higher inclinations.

We also study the effects of limited resolution on the inference capabilities of our model. We perform this study by executing the same comparison as done in Figure 3, but after convolving both the GRMHD images and the model images with a Gaussian beam of 10 μas FWHM during the fitting process. This blurring kernel approximates the results of imaging EHT sources. A summary of the results is shown in Figure 4.

The inverse relationship between the model's NxCORR scores and inclination still remains, although the overall performance of the model has improved. This indicates that our model accurately reproduces the structures in the images of time-averaged GRMHD that can be accessed with the resolution of current instruments. However, while the effect of blurring improves the NxCORR in the best fits, the parameter inference is worse, especially for θ_g and spin. This decrease in inference performance at lower resolutions indicates that our model's ability to infer mass and spin is likely sensitive to fine scale image structures that are no longer present after blurring. One possibility is the tendency for spin to cause small asymmetries in the black hole shadow (e.g., Takahashi 2004) and to introduce shifts in the photon ring with respect to the direct emission (e.g., Papoutsis et al. 2023). These effects are diminished once the GRMHD models are

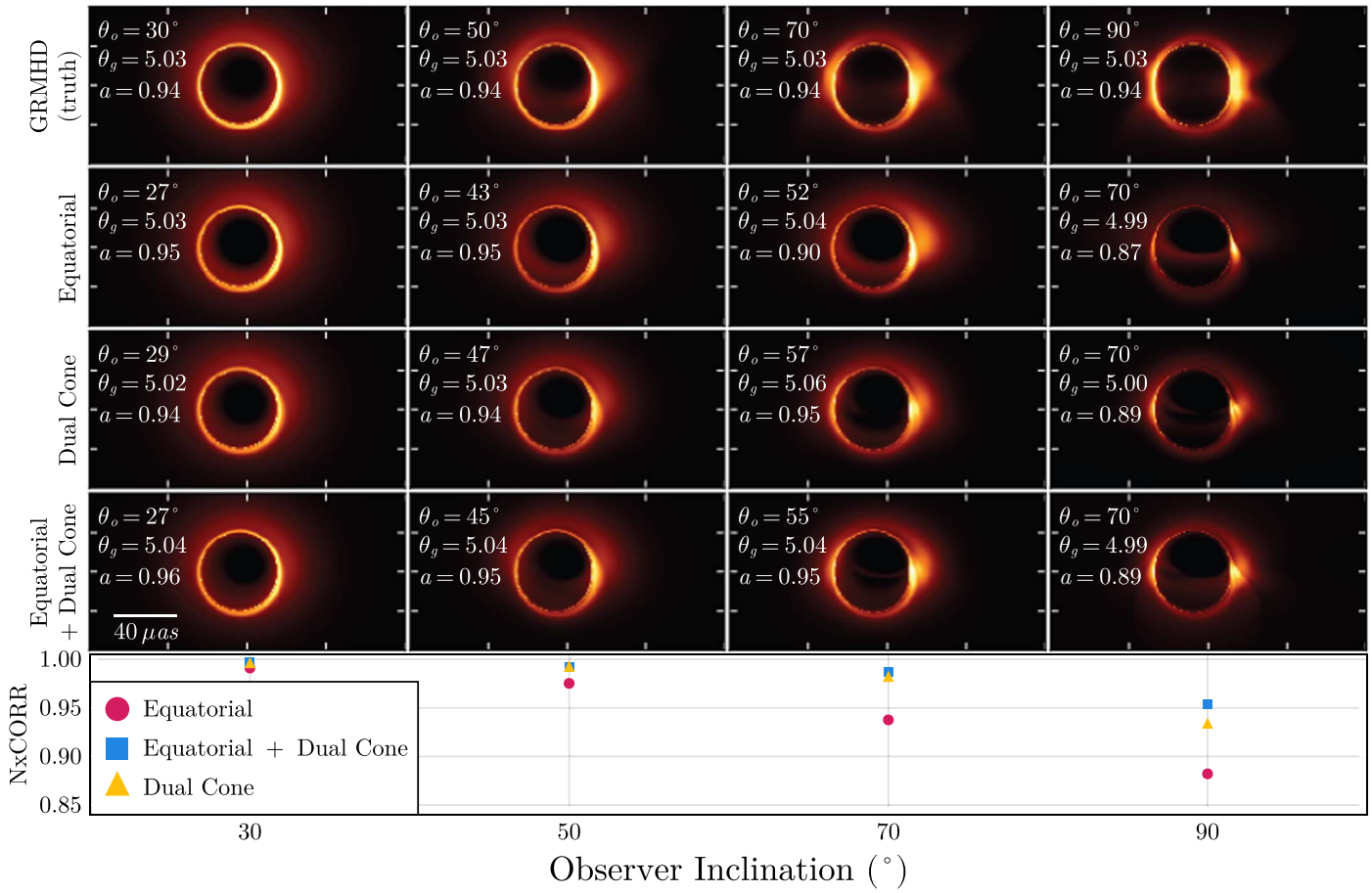

Figure 3. Best-fitting equatorial, dual-cone, and combination (equatorial + dual-cone) models to a time-averaged retrograde $R_{\rm high} = 160$ MAD GRMHD simulation of Sgr A* viewed at inclinations of 30°, 50°, 70°, and 90° (from left to right). The NxCORR score for all models is above 0.85 and increases as the black hole is viewed more face-on. In addition, the parameters of the best-fitting models are within a few percent of the true parameters for both mass and spin at low-to-modest inclinations. As expected, the dual-cone model (13 parameters) outperforms the equatorial model (12 parameters) despite having only a single additional parameter. In contrast, the combination model (23 parameters) provides only marginal additional improvement despite nearly doubling the number of parameters. Table 4 lists the parameters for each model.

blurred to EHT resolutions. Features that largely survive blurring include the brightness asymmetry and apparent shadow diameter. The shadow diameter is mostly consistent at all inclinations, which suggests that the model's ability to infer the true inclination is likely dependent on the morphology of the brightness distribution in the image. A discussion on our sensitivity of the model's parameters to various image features can be found in Appendix A.1.

We emphasize that these simple dual-cone emission models provide accurate representations of the image-domain morphology of time-averaged GRMHD, even when blurred to EHT resolution. Figure 5 shows two representative examples of a best-fit NxCORR dual-cone model along with its truth image at native resolution and after being blurred by a 10 FWHM Gaussian beam. The intensity profiles of the dual-cone model are strikingly similar to the truth, especially along the photon ring region. This is an interesting result since the dual-cone model is taken to be completely optically thin, and thus would be expected to produce generically brighter photon rings than what would be seen from a more accurate model with optical depth effects, such as GRMHD. These considerations indicate some degeneracy between the optical depth effects of radiative transfer and the emission physics of our models. For example, our optically thin model may exploit the anisotropy of synchrotron emission to replicate the impact of optical depth on tuning the relative flux between the photon rings of models with different emission physics. It is then possible for anisotropy effects to partition the flux of emitters away from the $n = 1$ direction, causing the $n = 1$ ring to appear dimmer than would be expected (see Gates et al. 2021 for an example of how emission anisotropy can affect the total flux seen by an observer at infinity from equatorial emitters; and Figure 3 of Bardeen & Cunningham 1973 for an example of how flux in the $n = 0$ and $n = 1$ images are partitioned by emission direction).

4. Bayesian Inference in the Visibility Domain

VLBI observations of a source give rise to sparse data products in the Fourier domain of an image. Thus, interpreting VLBI data is reliant on a source model, regardless of whether the model's purpose is imaging or parameter extraction. The EHTC has used many approaches to produce images from VLBI observations (see, e.g., M87* IV, Sgr A* IV). While flexible, these algorithms are only able to constrain the image-domain structure and not the physical source parameters (e.g., black hole mass and spin) directly. Therefore, converting simple geometric properties of the data/images, such as ring size, shape, and width, to intrinsic properties of the physical system requires calibration.

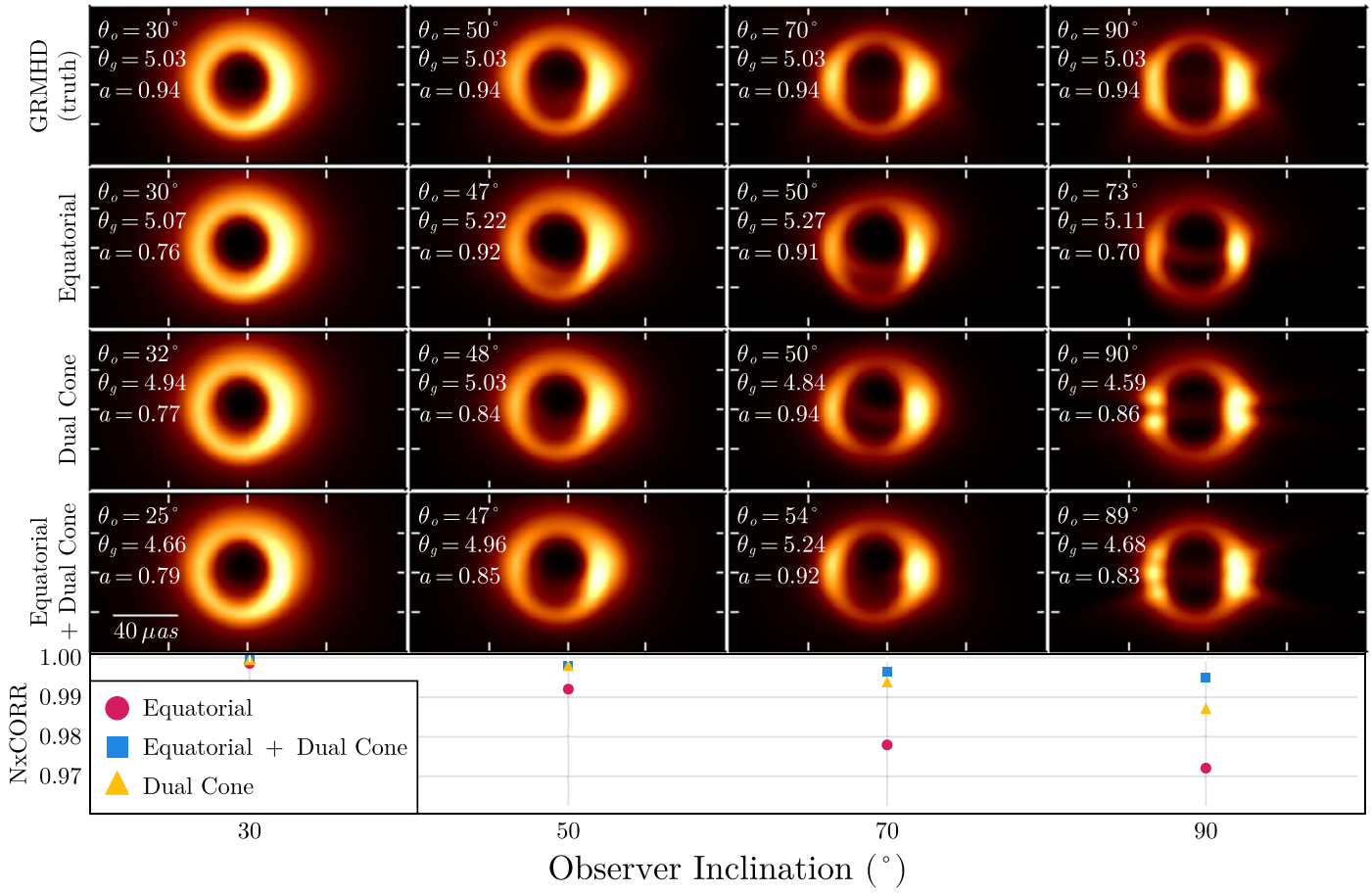

Figure 4. Same as Figure 3, but when the ground truth image and model image are both blurred by a 10 μas FWHM Gaussian kernel before comparison. The resulting NxCORR values are higher than for the unblurred case, with excellent fidelity for all model types. However, despite the improved image fidelity at this resolution, the best-fitting parameters have significantly larger discrepancies than for the unblurred fits, showing the strong degeneracies that are present when restricted to the current EHT resolution, especially because the photon ring cannot be distinguished from the direct emission.

In M87* (VI), Sgr A* (IV), and Sgr A* (VI), a calibration procedure called α-calibration was used to move from the ring size to the mass of the central black hole. By creating a large number of synthetic data sets of GRMHD snapshots, each imaging or geometric modeling pipeline was able to relate the reconstructed diameter $\hat{d}$ to the intrinsic gravitational radius of the system θ_g using the equation

$$d = \alpha\theta_g, \tag{27}$$

recovering a GRMHD-based calibration for α, and relating the measured ring size of M87*/Sgr A* to the mass of the central black hole.

However, this analysis is not ideal. In particular, it is likely that significant information from the black hole's influence on its image is not incorporated into the calibration procedure since it only uses the single parameter for the ring diameter. Any imposed constraints from additional relativistic features are not translated through the α-calibration into the GRMHD solution space.

An ideal analysis would involve directly fitting dynamic accretion models to data, for example, directly fitting GRMHD and all of its accretion and emission parameters. Unfortunately, the ability to conduct such an analysis with GRMHD was and is likely infeasible due to the computational complexity of directly sampling the solution space.

Following Palumbo et al. (2022), we avoid the two-step procedure of imaging followed by α-calibration by using our dual-cone model as a method to infer physical parameters directly from VLBI data. We first perform a Bayesian inference study of the dual-cone model, using two different data sets. The first is generated from a synthetic observation of an instantiation of the dual-cone model. For this test, we use the model that has the best NxCORR when fit to the $R_{\rm high} = 160$ SANE GRMHD of Figure 2 whose flux had been normalized to that of the GRMHD simulation that it was fitted from. A study on this data is important for understanding degeneracies that may exist when performing inference on realistic data. The second data set comes from a synthetic observation of the $R_{\rm high} = 160$ SANE GRMHD simulation that was used to create the previously mentioned model instance. This data set allows us to compare the visibility-domain fits to the image-domain NxCORR analysis to understand how the limited coverage of the EHT affects inferred parameters. Finally, we use data from the public release of the EHT 2017 April 6 observations of M87* to perform a Bayesian parameter inference study on M87*. This sequence of tests allows us to assess the successes and shortcomings of our model under a variety of increasingly challenging (and realistic) circumstances, with increasing degrees of known and unknown model errors. We report corner plots of the parameter posteriors for all fits, and report the highest probability density interval (HPDI) of each

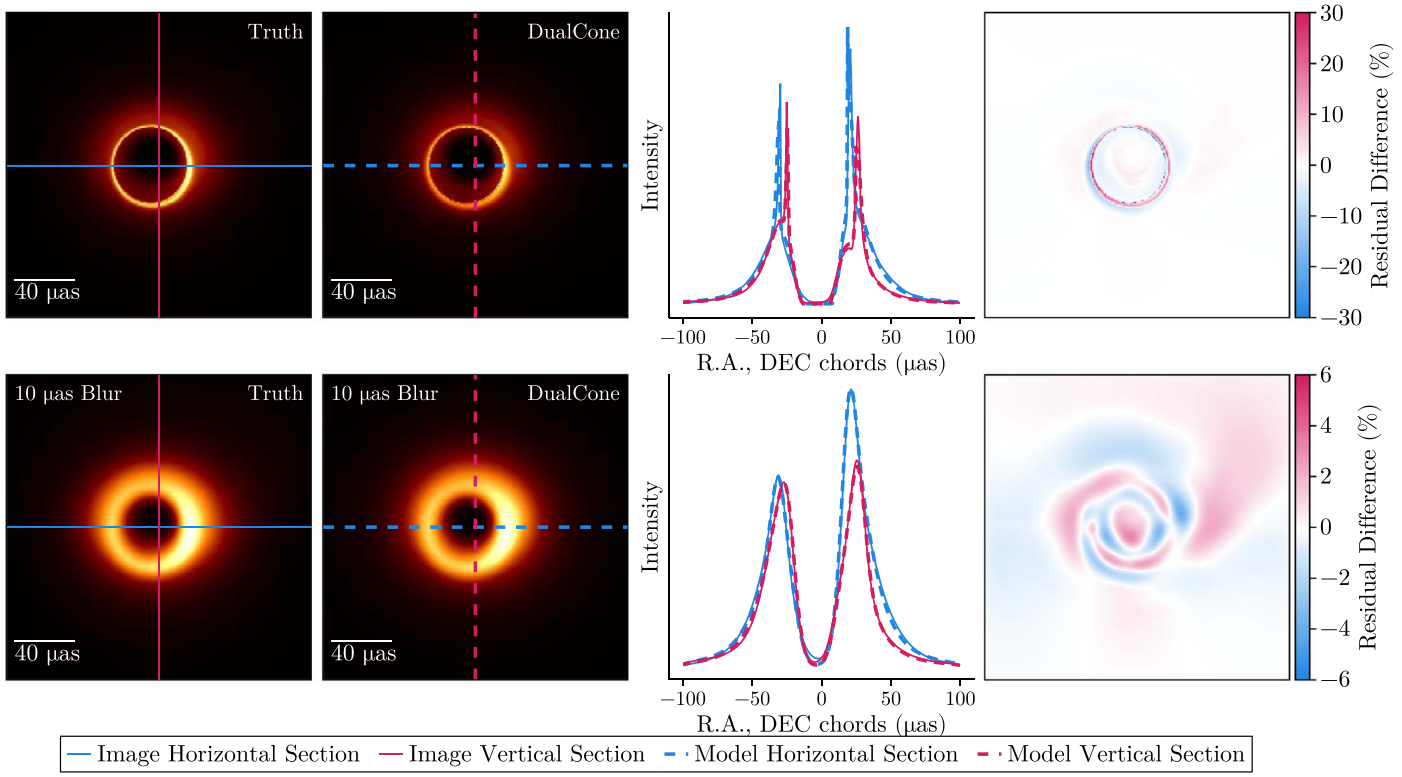

Figure 5. Comparison of a time-averaged GRMHD image with the best-fit dual-cone model, both at native resolution (top) and after being blurred by a 10 μas FWHM Gaussian beam (bottom). The simulation corresponds to a retrograde, $R_{\rm high} = 160$, MAD simulation of Sgr A*. Columns show the GRMHD image (left), the best-fit model (left center), horizontal and vertical intensity cross sections (right center), and residual images as a fraction of peak intensity (right).

parameter, which is the smallest interval of a parameter that contains 95% of the posterior mass.

4.1. Data Products

The ideal visibilities of a source are related to image intensities, $P(x, y)$, through a Fourier transform,

$$\mathcal{V}_{ij}(u_{ij}, v_{ij}) = \iint \mathrm{e}^{-2\pi i(u_{ij}x + v_{ij}y)} P(x, y)\, dx\, dy, \tag{28}$$

where i, j indexes the two sites that make up the baseline at the point (u_{ij}, v_{ij}) in visibility space, and (x, y) are the horizontal and vertical screen coordinates. However, the ideal visibilities differ from the observed visibilities due to the additional effects of noise and site-specific corruptions (called "gains"). In particular, the observed visibilities, $V_{ij}(u_{ij}, v_{ij})$ are related to the ideal visibilities through the relationship

$$V_{ij} = g_i g_j^* \mathcal{V}_{ij} + \epsilon_{ij} = |V_{ij}|\ e^{i\phi_{ij}}, \tag{29}$$

where g_i is the site-specific gain corruptions (Thompson et al. 2017). The gain corruptions, g_i, are effectively modeled as complex numbers that act independently at each site.[7] One can then define gain invariant quantities from closed triangles and quadrangles of visibilities. These gain invariant quantities are the closure phases,

$$\psi_{ijk} = \arg\left(V_{ij} V_{jk} V_{ki}\right) = \phi_{ij} + \phi_{jk} + \phi_{ki}, \tag{30}$$

and log closure amplitudes,

$$c_{ijkl} = \ln \left| \frac{V_{ij} V_{kl}}{V_{ik} V_{jl}} \right| = a_{ij} + a_{kl} - a_{ik} - a_{jl}. \tag{31}$$

The ϕ_{ij} and a_{ij} are the visibility phases and log visibility amplitudes, respectively, and are related to the observed complex visibilities by

$$V_{ij} = \exp(a_{ij} + i\phi_{ij}). \tag{32}$$

These closure quantities have been used by many authors in past analyses of EHT data (e.g., Chael et al. 2018; EHTC et al. 2019a, 2019b, 2019e; Narayan et al. 2021; Lockhart & Gralla 2022; Medeiros et al. 2023).

We generate the visibilities for the data sets used in the self-fit and GRMHD fits with the `observe_same` functionality of `eht-imaging` to mimic EHT-like coverage from the April 6 observations of M87*. All data used have been averaged over each scan using the `scan_average` functionality of `Pyeht-tim`, a `julia` wrapper of the Python library `eht-imaging`. Since the large-scale structure around M87*, which we do not model, is over-resolved by the EHT array, we flag visibilities with $u - v$ distances shorter than 0.1 Gλ. All visibility data products of the dual-cone model in this section are generated from 180×180 pixel images on a 120×120 μas field of view.

4.2. Log-likelihoods

The likelihoods for a set of nonredundant closure quantities can be constructed under the assumption that they are characterized by a multivariate Gaussian distribution (Blackburn et al. 2020). The closure amplitude likelihoods, in

[7] Interestingly, site-specific corruptions allow for an interpretation of the observed visibilities as a discontinuous field with a local GL(1, $\mathbb{C}$) symmetry (Thyagarajan et al. 2022).

particular, can be written as

$$\mathcal{L}(\boldsymbol{c}|\hat{c}) \propto \exp\left[-\frac{1}{2}\tilde{\boldsymbol{c}}^{\top}\boldsymbol{\Sigma}_{\mathbf{c}}^{-1}\tilde{\boldsymbol{c}}\right], \tag{33}$$

where $\tilde{\boldsymbol{c}} = \boldsymbol{c} - \hat{c}$ are a vector of residual closure amplitudes between the measured $\boldsymbol{c}$ and the model hypothesis $\hat{c}$, and $\Sigma_{\mathbf{c}}$ is the covariance matrix of $\boldsymbol{c}$. The likelihood for closure phases can be constructed similarly from their complex exponentials. We define

$$\mathbf{e}(\boldsymbol{\Psi}) = \exp(i\boldsymbol{\Psi}) \tag{34}$$

to be a vector of complex exponentials formed from its element-wise action on vector of closure phases Ψ. The likelihood is then

$$\mathcal{L}(\boldsymbol{\Psi}|\tilde{\boldsymbol{\Psi}}) \propto \exp\left[-\frac{1}{2}\tilde{\boldsymbol{e}}^{\dagger}\boldsymbol{\Sigma}_{\mathbf{e}}^{-1}\tilde{\boldsymbol{e}}\right], \tag{35}$$

where we have chosen this form to account for the phase wrapping in ψ. We do not include the data-dependent normalization coefficients of the likelihood functions since they contribute an overall constant to our posterior densities and, thus, do not influence inference.

4.3. Priors

We generally take broad, flat priors on our model to reflect our ignorance of the source. Mass estimates of M87* from stellar dynamics and gas dynamics methods are typically dependent on the distance from the Earth to M87*. The quantity constrained by each method is the mass-to-distance ratio, θ_g. We, therefore, choose to report the measured θ_g of the source instead of its mass.

The literature features widely discrepant measurements for θ_g. These measurements range from their smallest value of $\sim$2 μas, from the gas dynamics methods to their largest of $\sim$6 μas, and from the largest stellar dynamics measurements. We therefore adopt wide priors on θ_g to encompass all of these, ranging from 1 to 8 μas.

Priors on the spin of M87* can be taken from properties of the large-scale jet and horizon-scale images of M87*. We will assume that the orientation of the spin axis is related to the inclination and p.a. of the large-scale jet. Studies of the jet dynamics of M87* suggest an inclination of $\sim$17° from the line of sight, while images of the large-scale jet imply a p.a. of 288° from north (e.g., Mertens et al. 2016; Walker et al. 2018). Horizon-scale images of M87* show a peak brightness in the south, indicating that the spin of M87* points away from our line of sight (M87* V). We incorporate these observations into our prior by fixing the observer's inclination to lie strictly within a range of $\sim$20° around the observed large-scale jet inclination, $\theta_o \in [1°, 40°]$, and fixing the spin to take on only negative values with the full range of magnitudes, $a \in [-1, 0)$. Since the large-scale jet is observed to point in a westerly direction on sky, the p.a. shift is restricted to lie at a range of p.a. $\in [-\pi, 0]$. A description of all the priors used in the analyses of this section is given in Table 1.

4.4. Sampling

Our Bayesian analysis was performed within `Comrade.jl`, a VLBI statistical inference framework (Tiede 2022). Posterior sampling was performed with `Pigeons.jl` (Surjanovic et al. 2023), a `Julia` (Bezanson et al. 2017) implementation of a nonreversible parallel tempering algorithm (Syed et al. 2021). We use the default slice sampler for the kernel of the exploration step (Neal 2003).

Table 1
Model Parameters and Prior Ranges Used in the Bayesian Analyses with the Dual-cone Model (Section 4)

Parameter	Description	Units	Prior
θ_g	Mass-to-distance ratio	μas	$\mathcal{U}(1.5, 8)$
a	Black hole dimensionless spin	…	$\mathcal{U}(-1, 0)$
θ_o	Observer inclination	rad	$\mathcal{U}\left(1, \frac{40}{180}\pi\right)$
θ_s	Cone opening angle	rad	$\mathcal{U}\left(\frac{40}{180}\pi, \frac{\pi}{2}\right)$
p.a.	Position angle of projected spin axis	rad	$\mathcal{U}(-\pi, 0)$
R	Characteristic radius of intensity profile	$\frac{GM}{c^2}$	$\mathcal{U}(1, 18)$
p_1	Inner exponent of intensity profile	…	$\mathcal{U}(0.1, 10)$
p_2	Outer exponent of intensity profile	…	$\mathcal{U}(1, 10)$
χ	Fluid velocity azimuthal angle in ZAMO frame	rad	$\mathcal{U}(-\pi, \pi)$
ι	Magnetic field orthogonality angle in fluid frame	rad	$\mathcal{U}(0, \frac{\pi}{2})$
β	Fluid speed in ZAMO frame	c	$\mathcal{U}(0, 0.9)$
σ	Spectral index of emission	…	$\mathcal{U}(-1, 3)$
η	Magnetic field tangential angle in fluid frame	rad	$\mathcal{U}(-\pi, \pi)$

Table 2
Highest Probability Density Interval (HPDI), the Smallest Interval Containing 95% of the Posterior Weights, of Modes 1 and 2 from the Posterior Samples of Our Dual-cone Model Fitted to a Time-averaged, Prograde, SANE GRMHD Simulation with $R_{\rm high} = 160$

Param.	Cluster 1		Cluster 2	
	Low	High	Low	High
m_d	1.50	2.93	3.23	5.21
a	−1.00	−0.06	−1.00	−0.28
θ_o (deg)	10	30	9	29
θ_s (deg)	40	62	45	60
p.a. (deg)	275	306	283	332
R	4.76	15.10	1.00	4.91
p_1	0.87	9.71	0.10	9.46
p_2	4.77	7.34	3.75	6.36
χ (deg)	−140	−56	−104	32
ι (deg)	10	90	37	90
β_v	0.36	0.90	0.18	0.82
σ	0.48	4.96	0.46	4.80
η (deg)	−142	93	−131	80

4.5. Visibility-domain Fit: Dual-cone Model

This section features the results of a self-fitting exercise to synthetic data generated from our model. The fitted HPDI of each parameter of this analysis is shown in Table 2. The synthetic data are generated using the coverage and the measured thermal noise of the 2017 April 6 EHT observations of M87*. Figure 6 shows a corner plot of the mass-to-distance ratio, spin, spin axis inclination, jet opening angle, spin axis p.a., and characteristic radius of the emissivity function (θ_g, a, θ_o, θ_s, p.a., and R) of samples from the posterior.

The true image of the model used in this analysis features two disjoint ring features, which are blended together at the nominal resolution of the EHT. This blending introduces

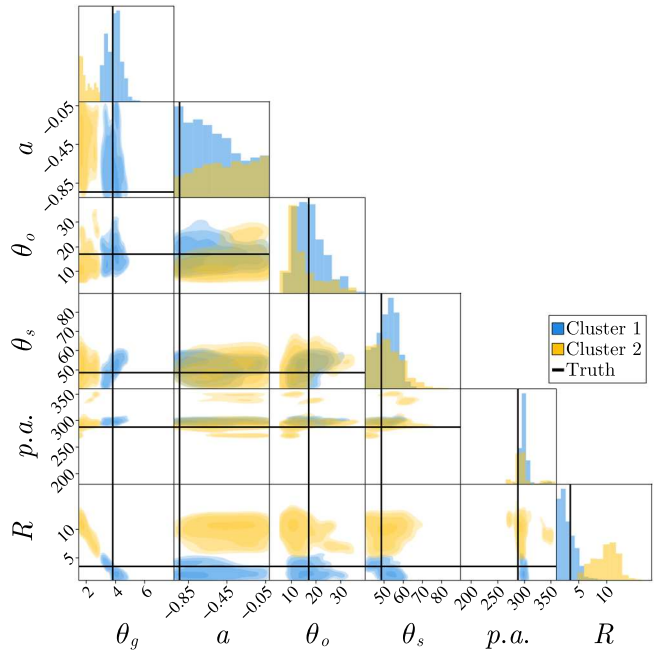

Figure 6. Partial corner plot showing the posterior for a subset of the parameter space of a dual-cone fit to itself using EHT 2017 coverage. The shown parameters are the mass-to-distance ratio (θ_g), the black hole spin (a), the observer inclination (θ_o), the jet opening angle (θ_s), the projected position angle of the spin axis on the observer's screen (p.a.), and the characteristic radius of the emissivity function (R). The true values of the model used to generate the data are shown with black lines. The posterior features two distinct clusters, depicted in blue and yellow, which we isolate using the k-means clustering algorithm. Figure 16 shows the full corner plot for this fit.

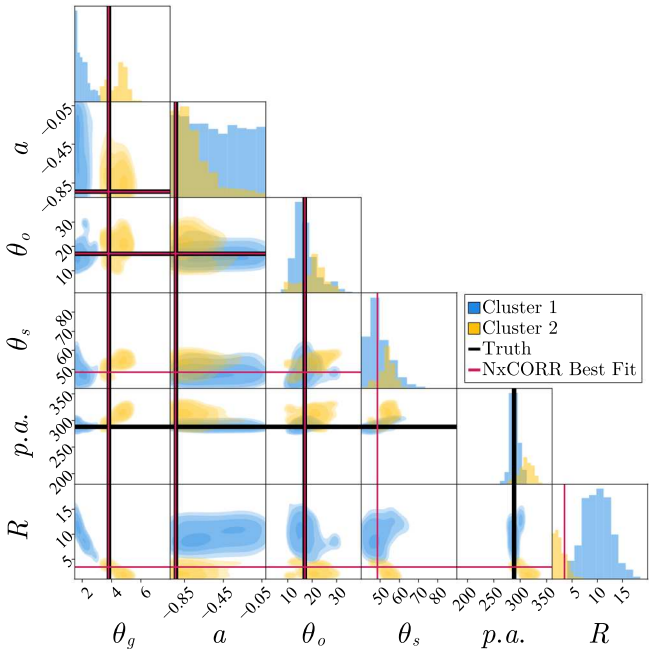

Figure 7. Partial corner plot showing the mass-to-distance ratio (θ_g), the black hole spin (a), the observer inclination (θ_o), the jet opening angle (θ_s), the projected position angle of the spin axis on the observer's screen (p.a.), and the characteristic radius of the emissivity function (R). The true values of the GRMHD simulation are shown with black lines; the values inferred from by the model in our image-domain NxCORR fit of Section 3 are shown in red. Figure 17 shows the full corner plot for this fit. The posterior features two distinct clusters, depicted in blue and yellow, which we isolate using the k-means clustering algorithm.

degeneracies in the posterior when fitting. We study these degeneracies by collecting the samples into two clusters with a k-means algorithm on θ_g. The clusters defined by k-means minimizes the sum of the squared distances from the cluster's mean for each point in the cluster. Since θ_g acts as a scaling parameter on the image, the panels of Figure 6 depicting the joint posterior with θ_g (leftmost column) show the influence of various modeling parameters on the image size. Other than θ_g, the parameter that appears to have the most direct effect on the image size is the characteristic radius R, as is evident from the inverse relationship between the two parameters seen in the bottom left panel of the plot. A similar trend is seen in the posterior fits of Palumbo et al. (2022). We also note that the clusters with smaller values of θ_g are biased toward larger values of spin. The biasing is likely due to the contribution of the photon ring to the overall flux of the image since spin can have a small effect on the photon ring's size. The contribution, however, appears to be weakly constrained since the spin distributions in each cluster are still broad.

4.6. Visibility-domain Fit: GRMHD

In this subsection, we study the fit of our dual-cone model to synthetic observations generated from the prograde, SANE GRMHD model of Figure 2. The main results of this section are summarized in Figure 7, which shows the posterior samples for some parameters of interest, which we have classified into two distinct clusters on θ_g with the k-means clustering algorithm. The true "on-sky" GRMHD image is shown in the first column of Figure 8, while the second and third columns show representative images from each cluster at their true resolution (upper row) and at the EHT nominal resolution of

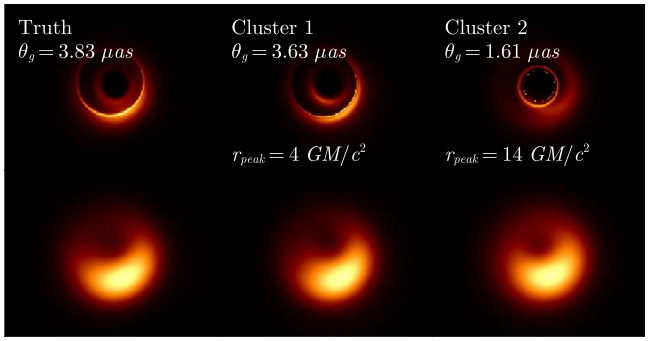

Figure 8. True image of the GRMHD simulation (left) with samples from the GRMHD posterior from each mode of the posterior (center and right). The top row shows images at the native resolution used to generate the data; the bottom row shows the same images after being blurred to the nominal EHT resolution of 20 μas. All images feature a disjoint double ring structure that is not discernible when seen at the EHT nominal resolution.

20 μas (lower row). A corner plot of all parameters with their posterior samples can be found in Figure 17.

Most images generated from the posterior samples feature two disjoint rings as also seen in the true image. An inspection of the lower left panel of Figure 7 indicates that Cluster 1 is associated with black holes of smaller mass and larger emission radii while Cluster 2 is associated with black holes of larger mass and smaller emission radii. For the first cluster, the decomposition of $n = 0$ and $n = 1$ emission matches the ground truth image better and is visually similar to the results from Section 3. For the second cluster, the $n = 1$ emission of the dual-cone model focuses on the emission from the jet funnel of

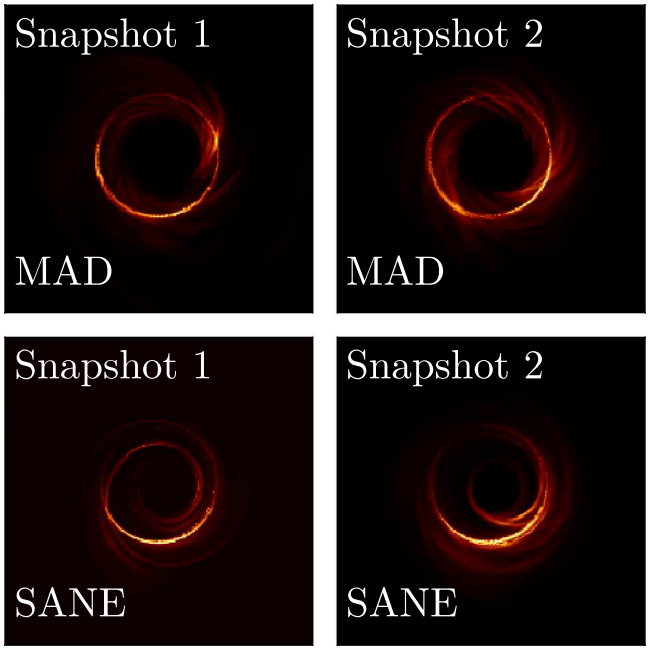

Figure 9. Snapshots of an $R_{\rm high} = 20$ simulation of a MAD accretion flow (top) and an $R_{\rm high} = 160$ simulation of a SANE accretion flow (bottom). These snapshots were used to produce data for the model fits shown in Figure 10.

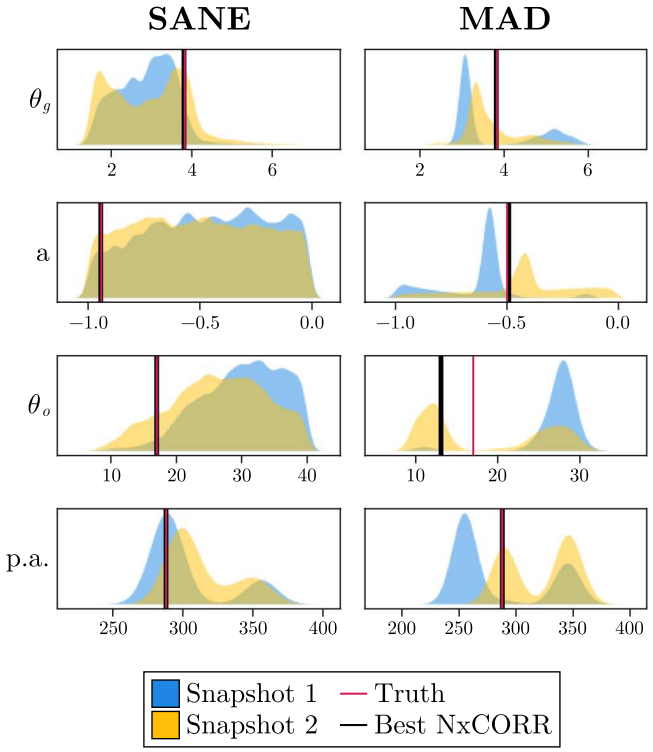

Figure 10. Marginalized posteriors for snapshot fits to a $R_{\rm high} = 160$ SANE simulation (left) and $R_{\rm high} = 20$ MAD simulation (right). The distributions of two snapshot fits to each simulation are shown in blue and yellow. The parameters shown are the mass-to-distance ratio (θ_g), spin (a), spin axis inclination with respect to the observer (θ_o), and the spin axis position angle (p. a.). For each parameter, the true values and the best NxCORR values that were taken from fits to the time-averaged model in Section 3 are shown with red and black vertical lines, respectively.

the SANE simulation. These two clusters illustrate a degeneracy that occurs between the emission radius and black hole mass that is consistent with the results from Palumbo et al. (2022).

This multicluster posterior is a consequence of the finite angular resolution of the EHT array, as is demonstrated by the lower row of Figure 8. After blurring to the nominal EHT resolution of 20 μas, both clusters appear identical and consistent with the blurred true image. We note that the image-domain fit of our model to the GRMHD simulation in Section 3 should act as a proxy for a visibility-domain fit at sub 1 μas resolution (matching the pixel resolution of the fitted images); in this case, the fit converges to a model whose image features a photon ring of the same size as the underlying GRMHD. Thus, we expect that arrays with sharper angular resolution than the EHT, sufficient to distinguish the primary emission ring and the photon ring, would resolve the multicluster degeneracy seen in the EHT fits.

Finally, despite the differences in appearance, both clusters predict a prograde inflow accretion with a significant scale height on the emission surface. These features are consistent with the image-domain analysis of Figure 2 and with the true simulation.

As in GRMHD simulations, the accretion flows in LLAGN are composed of turbulent plasma and are observed to be highly variable (see the conclusions of EHTC et al. 2019f). This variability introduces a source of misspecification for our model, and means that fits to "snapshots" will differ from fits to time-averaged images. Because the variability timescale for M87* is $\sim$ days, snapshot fits to GRMHD are an appropriate proxy for fits to EHT data from M87* over a single night.

To assess the effects of this time-variable structure, we fit our model to snapshots of both MAD and SANE simulations using our dual-cone model (see Figure 9). Figure 10 shows density plots for these fits. The results of these fits suggest that the systematic errors expected in our model could be dependent on the underlying accretion flow, with fits to snapshots of the SANE model showing less variance than the MAD fits. Notably, both snapshot fits to the SANE simulation contain the values of the best NxCORR representative model in the bulk of their posteriors. The MAD fits, in contrast, have a larger variance between the two posteriors, with only one posterior containing all values of the best NxCORR representative model in its bulk.

4.7. Visibility-domain Fit: EHT Data

We also used our model to fit EHT observations on M87*. In this case, the limitations of model errors are unknown, but we can still evaluate the ability of the model to reproduce actual measurements. Nevertheless, while we have shown that our model accurately represents time-averaged GRMHD with reasonable parameters, realistic data will include degrees of freedom not included in the dual-cone model. For instance, GRMHD simulations show significant structural turbulence in snapshots. These turbulent structures are not captured in our dual-cone model and may introduce systematic errors, as previously discussed in Section 4.6.

We conduct our analysis on the April 6 observations of M87*, following M87* V. Figure 11 summarizes our results; the full posterior samples can be found in Figure 18. The 95% HPDI for the parameters of our model is shown in Table 3. We infer a relatively narrow posterior for the mass-to-distance ratio $\theta_g \in (2.84, 3.75)$ from our fits, consistent with the stellar mass estimates of Gebhardt et al. (2011), EHTC et al. (2019b), and

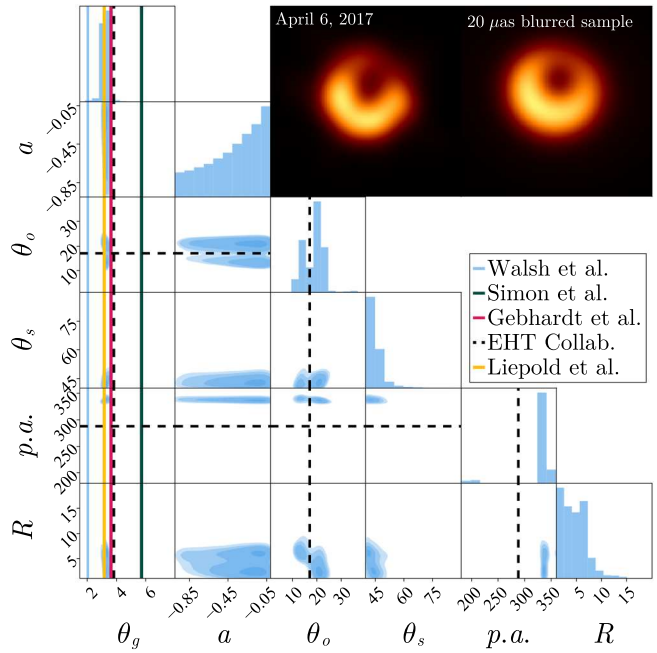

Figure 11. Partial corner plot for a dual-cone fit to the 2017 April 6 EHT observations of M87*. The shown parameters are the mass-to-distance ratio (θ_g), the black hole spin (a), the observer inclination (θ_o), the jet opening angle (θ_s), the projected position angle of the spin axis on the observer's screen (p.a.), and the characteristic radius of the emissivity function (R). Vertical lines show other mass measurements of M87* in red (Gebhardt et al. 2011), blue (Walsh et al. 2013), black dotted M87* (VI), yellow (Liepold et al. 2023), and green (Simon et al. 2023). We also show the measured position angle and inclination of the large-scale jet in M87* (Walker et al. 2018). The inset images show the consensus April 6 image of M87* reported by the EHTC and a random sample drawn from the posterior, blurred with a 20 μas FWHM Gaussian beam. Both images have their peak brightness in the southeastern quadrant.

Liepold et al. (2023). In contrast to θ_g, our spin inference is weakly constrained, a result that is consistent with the results of the previous self-fit and GRMHD fit. Our inability to constrain the black hole spin with our model, even when performing self-fits, suggests that spin measurements with the 2017 EHT array are infeasible. Furthermore, restricting the priors on the emission geometry would not improve the spin constraints significantly since the emission parameters are uncorrelated with spin for Stokes I. The lack of correlation of spin, at EHT resolution, with any of the model parameters is evident from the structure of the posteriors in the spin columns of Figures 17 and 18, and holds even in the self-fit of Figure 16.

A spin measurement that relies on Stokes I quantities will likely require improved resolution or sensitivity to dynamical signatures to discern the effects of spacetime from accretion. Future proposed VLBI arrays, such as extensions of the EHT to space with the Black Hole Explorer, will aim to measure the $n = 1$ photon ring directly, providing an avenue to Stokes I spin measurements. At the resolution of the EHT, including polarization data may improve the prospects of spin constraints due to frame-dragging effects on the polarization pattern (Palumbo et al. 2020; Palumbo & Wong 2022; Chael et al. 2023) and improved astrophysical constraints (e.g., M87* VIII, M87* IX, Sgr A* VIII).

Although we are unable to constrain the magnitude of the spin from our model, we measure a spin axis inclination that is consistent with the direction of the large-scale jet, $\theta_o \in (11°, 24°)$ (Walker et al. 2018). In contrast, the EHTC analysis of

Table 3
95% Highest Probability Density Interval (HPDI) of Our Dual-cone Model Fitted to Closure Quantities of M87* Taken from the EHTC Observations on 2017 April 6

Param.	Low				High	
θ_g	2.84				3.75	
a	−0.90				−0.01	
θ_o (deg)	11				24	
θ_s (deg)	40				56	
p.a. (deg)	200				347	
R	1.00				8.46	
p_1	0.71				9.99	
p_2	1.47				7.27	
χ (deg)	35				140	
β_v	0.08				0.55	
ι (deg)	10				49	
	Cluster 1		**Cluster 2**		**Cluster 3**	
	Low	**High**	**Low**	**High**	**Low**	**High**
σ	1.73	5.00	1.29	3.95	2.98	5.00
η (deg)	−19	27	151	180	−180	−149

Note. The posterior features three modes in η. These modes have largely similar HPDI except for their spectral indices, which are shown separately. Although the HPDI reports a broad interval for the inferred p.a. of the projected spin axis, the distribution has two separate clusters in p.a., as can be seen in Figure 6, which excludes the truth.

M87* was performed by assuming that the spin axis is aligned with the large-scale jet. Misaligned disks are, however, believed to be a generic feature of many AGN, with some authors arguing for a tilted flow in the M87* system from the wobbling of the large-scale jet (e.g., Cui et al. 2023), so this independent measurement of inclination is both encouraging for the EHTC conclusions and nontrivial.

We emphasize, however, that our model makes this inference under the assumption that the spin axis is aligned with the symmetry axis of the horizon-scale accretion flow. One can expect an alignment of the horizon-scale accretion flow with the spin axis of the black hole from the Bardeen–Petterson effect, which applies a torque to misaligned viscous flows (Bardeen & Petterson 1975; Thorne et al. 1986). GRMHD simulations often do not include a viscosity term in their evolution, but the presence of the magnetic field appears to introduce an effective viscosity to the fluid that has been seen to align flows in simulations that feature tilted disks (see, for example, the tilted disk simulations of Liska et al. 2019). This effect is typically seen to occur within a few tens of gravitational radii of the hole, where the bulk of the emission observed by the EHT originates.

Despite the forced alignment, the presence of a tilted flow can still leave imprints on images of GRMHD through its effect on the jet, although some of these features are suppressed at the 230 GHz frequencies observed by the EHT (Chatterjee et al. 2020). In particular, the shape of the photon ring appears largely unaffected. It is thus reasonable to expect that our model should still be sensitive to the inclination of the spin of the black hole, rather than the inclination of the large-scale accretion.

We also infer a projected p.a. of the spin axis that points more northerly than would be expected if it was aligned with the large-scale jet (see Figure 11). Studies on additional

observing epochs will be necessary to clarify whether this could be driven by a transient emission structure.

The design of our model allows us to infer the 3D emission geometry of our source. We infer an emission profile with a characteristic radius $R \in (1, 8.46)$, inner exponent $p_1 \in (0.71, 9.99)$, and outer exponent $p_2 \in (1.47, 7.27)$. From Equation (2), we can infer a peak radius,

$$R_{\rm peak} = R\left(\frac{p_1}{p_2}\right)^{\frac{1}{p_1+p_2}}, \tag{36}$$

which corresponds to a peak radius in the range $R_{\rm peak} \in (0.84, 10.40)$ that is similar to GRMHD simulations (Dexter et al. 2012; EHTC et al. 2019f; Emami et al. 2023). Our fitted emissivity parameters suggest that the emission geometry has a half-opening angle of $\theta_s \in (40°, 56°)$. The inferred accretion flow is inferred to be slow-to-moderately relativistic and retrograde, $\beta_v \in (0.08, 0.55)$, although we are unable to constrain whether it is inflowing or outflowing. Finally, we are unable to constrain aspects of the spectral index and magnetic field geometry tightly. There are many opportunities to verify these broad conclusions through additional data, including EHT observations of M87* in other years M87*-2018-I, as well as fits using multifrequency data and polarization information (M87* VII, M87* VIII, M87* IX).

5. Summary

We have introduced a semianalytic model for emission concentrated within a conical region near a black hole. Despite its simplicity, we have demonstrated that this model provides excellent approximations to a wide variety of time-averaged GRMHD simulations. Moreover, our model successfully achieves the goal of photogrammetry by capturing the properties of both the black hole and the surrounding emission when fit to high-resolution images or interferometric data.

Our model is highly efficient, both in terms of the expense to generate images (e.g., we are able to generate 400×400 pixel images in $\approx 10\ \mu$s with the integrated GPU on a laptop with the Apple M1 architecture) and in providing a low-dimension representation of horizon-scale images from LLAGN. For instance, our dual-cone model has only 13 parameter; for comparison, the `xs-ringauss` geometric model used by the EHT for their mass measurement of M87* requires 26 parameters (M87* VI). A further benefit of dual-cone model fits is that they directly measure physically relevant parameters (e.g., the black hole mass and spin, and properties of the emitting plasma), while the geometric model fits require an additional layer of analysis to interpret their parameters (e.g., the α-calibration procedure used in the EHTC; see Section 1).

We show that our model is capable of reproducing time-averaged images from a wide class of GRMHD simulations. Unlike previous semianalytic models that were restricted to equatorial emission, our model reproduces characteristic image morphologies that are seen in both SANE and MAD GRMHD simulations; they produce emission geometries that are broadly consistent with the true emission geometry of the underlying simulation, and are often able to discern the fluid direction (prograde or retrograde) from images.

We assess the suitability of our model for interpreting VLBI measurements using a series of tests that fit mock EHT observations of simulated images. We explore "self-fits" of the dual-cone model (Section 4.5) as well as fits to mock observations of both time-averaged and snapshot GRMHD images (Section 4.6). In both cases, the model fits give accurate mass measurements but do not meaningfully constrain the black hole spin, although we do see more significant biases from model misspecification in snapshot fits. These tests reinforce the EHTC conclusions that the spin cannot be measured from the current data without strong model assumptions.

We also used our dual-cone model to fit real EHT observations of M87*. As for the snapshot fits, we expect additional systematic errors from time-variable image structure (in addition to systematic errors from imperfections in the model specification). Nevertheless, these fits give estimates for the mass and inclination that are consistent with EHT measurements. However, we do see some evidence for systematic errors in the fits, including a p.a. for the black hole spin axis that differs from the direction of the large-scale jet.

Future extensions of the model could include linear and circular polarization, both of which provide important constraints in EHT analyses. They could also relax the assumption of axisymmetry, to directly model time-variable structures. Alternatively, a comparison of model fits over many gravitational timescales in M87* (e.g., over multiple years of EHT observations) will provide an empirical estimate for the systematic uncertainties associated with model misspecification and may provide guidance into what physical parameters can be confidently inferred from these fits.

Acknowledgments

We thank Koushik Chaterjee, Razieh Emami, Charles Gammie, Zachary Gelles, Sara Issaoun, Prashant Kocherlakota, Ramesh Narayan, Dominic Pesce, Angelo Ricarte, and George Wong for their insightful discussions. We acknowledge financial support from the Brinson Foundation, the Gordon and Betty Moore Foundation (GBMF-10423), and the National Science Foundation (AST-2307887, AST-1935980, and AST-2034306). This work was supported by the black hole Initiative, which is funded by grants from the John Templeton Foundation (grant No. 62286) and the Gordon and Betty Moore Foundation (grant GBMF-8273); all the opinions expressed in this work are those of the author(s) and do not necessarily reflect the views of these foundations. This work used the RCAC Anvil Cluster at Purdue University through allocation PHY230186 from the Advanced Cyberinfrastructure Coordination Ecosystem: Services & Support (ACCESS) program (Boerner et al. 2023), which is supported by National Science Foundation grant Nos. 2138259, 2138286, 2138307, 2137603, and 2138296.

Appendix A
Model Definition

A.1. Interpreting Model Parameters

Much of the interpretation of the dual-cone model parameters is gleaned from studies of the model's image structure. Here, we summarize some key features of the model to provide additional background and intuition. Figure 12 shows an example of what images of the model can look like for a random sample of emission parameters. The mass, spin, observer inclination, and p.a. are fixed. Two classes of images are generically formed whose classification depends on the observer's relative orientation with respect to the emission cone. These two classes fall broadly into the categories of

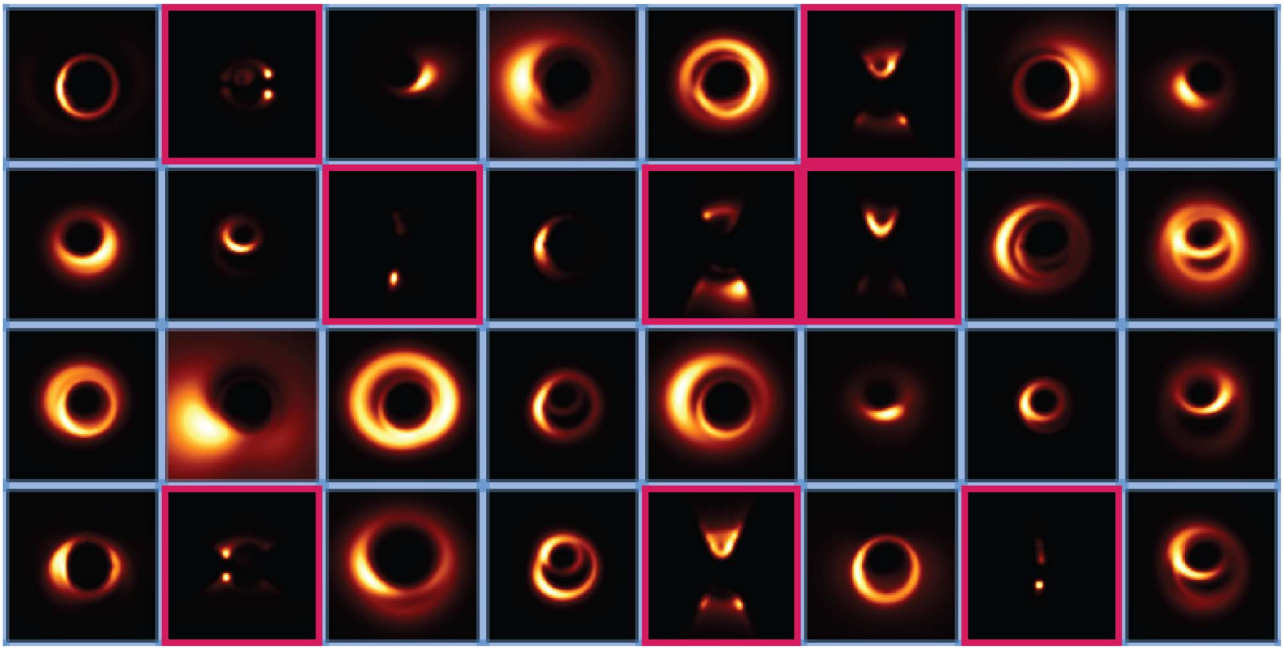

Figure 12. Random sample of images from the dual-cone model seen by a distant observer. All images shown are comprised of $n = 0$ and $n = 1$ subimages. In all images, the mass-to-distance ratio is the same, the observer inclination is 30°, the spin is -1, and the projected spin axis is oriented vertically on the observer's screen. The remaining parameters are sampled from a prior similar to Table 1, with the exception that the range of the cone opening angle has been extended to $\theta_s \in (0, \pi/2)$. We have classified the images into two categories, "inside the cone" (blue) and "outside the cone" (red). These are defined, respectively, by images generated with $|\cos\theta_s| < |\cos\theta_o|$ in the case of "inside the cone" images or $|\cos\theta_s| > |\cos\theta_o|$ in the case of "outside the cone" images.

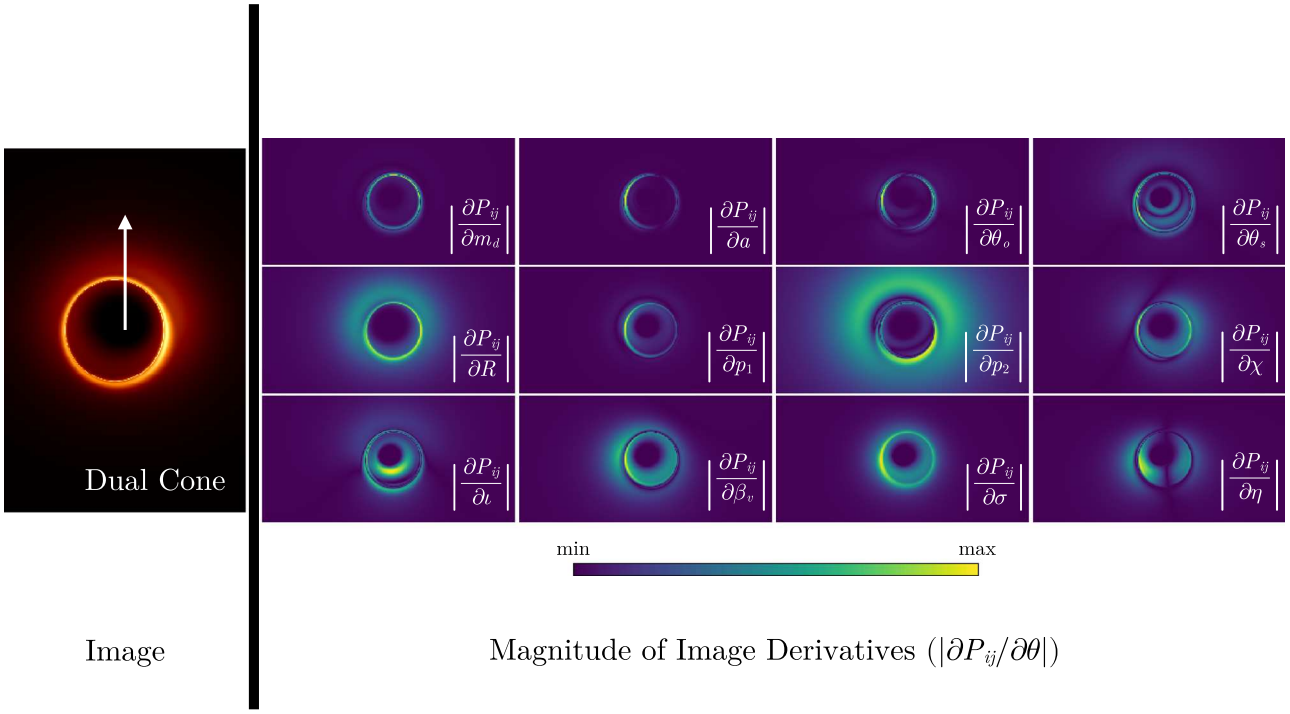

Figure 13. Assessing the influence of model parameters on various image features. The leftmost panel shows an image of one of the representative dual-cone models of Section 3. The direction of the spin is projected onto the image with a white arrow. The grid of panels to the right shows the magnitude of the partial derivatives of each image pixel with respect to the parameters of the dual-cone model. The color range in each of the derivative panels is rescaled to its minimum and maximum pixel value.

"inside the cone" or "outside the cone" and match that of Papoutsis et al. (2023). Observers who view the black hole with a configuration that satisfies $|\cos\theta_o| > |\cos\theta_s|$ see images in the "inside the cone" category, while observers viewing the black hole with a configuration $|\cos\theta_o| < |\cos\theta_s|$ see images in the "outside the cone" category. Figure 12 shows example images from each class, all featuring both $n = 0$ and $n = 1$ emission. Some of the "inside the cone" images depict only a single ring-like feature instead of multiple, which is emblematic of the flexibility of our anisotropic synchrotron-emission

model allowing for the peak intensity of the $n = 0$ image to be greater than that of $n = 1$, despite the fact that the dual-cone model is optically thin. Although our parameterization is axisymmetric, our emissivity model generically forms asymmetric emission structures in the bulk spacetime.

We give some intuition on how various parameters can affect features in the images of the model in Figure 13. This plot depicts gradients of the image pixels with respect to the model parameters when evaluated at one of the best-fit images in Section 3. The leftmost panel shows the true image with the direction of the projected spin axis superimposed as a white arrow. The parameters can broadly be categorized as spacetime-dependent parameters—the mass-to-distance ratio (θ_g), spin (a), and inclination (θ_o)—which are seen to have large gradients in only in the photon ring region, and emissivity and accretion parameters that largely affect features in either only the $n = 0$ subimage or both $n = 0$ and $n = 1$ subimages.

The image structure of spacetime-dependent gradients is consistent with the expected action of these parameters on the appearance of the photon ring. Papoutsis et al. (2023) have suggested, for example, that a shift in the photon ring with respect to the projected the spin axis is likely an observable sensitive to spin, since the $n = 0$ subimage is largely insensitive to spin. This effect can be seen in our spin derivative panel (first row, second column of the image gradients), which features a large gradient for emission in the $n = 1$ subimage and a relatively suppressed gradient for $n = 0$. The magnitude of the gradient is higher in regions of the $n = 1$ subimage that are away from the spin axis. The asymmetry in the sensitivity of the $n = 1$ feature to spin is indicative of the effect of spin on the photon ring's displacement. Another example is of the gradient with m_d (first row first column), which is also strongest in the photon ring region. The m_d parameter acts as a radial scaling of the black hole, a fact that is exemplified by the relatively uniform gradient around the $n = 1$ ring in the m_d panel.

Some of the emissivity parameters of interest are those that control the location of the peak emission R, p_1 and p_2. The magnitude of the derivative with respect to p_1 is peaked within a compact region, interior to the peak emission, while those of p_2 are peaked exterior to that region. These results are consistent with the definition of our emissivity envelope in Equation (2). Some of the accretion parameters, including fluid speed (β_v) and magnetic field azimuthal orientation (η) largely do not influence the $n = 1$ emission structure. We note that Figure 13 demonstrates that the "inner shadow" (Chael et al. 2021) is sensitive to the jet opening angle (θ_s) where the jet bases of the forward and rear jets are seen highlighted in the gradient with respect to θ_s.

A.2. Transformations of Quantities to Boyer–Lindquist Coordinates

Equation (6) can be used to map vectors in the ZAMO frame to vectors in the Boyer–Lindquist frame. Performing this transformation on the fluid velocity gives

$$u^{\mu} = u^{(m)} e_{(m)}{}^{\mu} = \beta_v \left(0, \sqrt{\frac{\Delta}{\Sigma_s}}\cos\chi, 0, \sqrt{\frac{\Sigma_s}{\Xi_s}}\frac{\sin\chi}{\sin\theta}\right), \quad \text{(A1)}$$

which shows that the intuition that χ controls the direction of the fluid flow carries over from the fluid frame to the global Boyer–Lindquist frame.

We can also transform the magnetic field vector in a similar fashion. Since there is no electric field in the fluid frame, a magnetic field four-vector can be constructed from $B^{m'}$ to find the magnetic field in the global Boyer–Lindquist frame (Gammie et al. 2003),

$$b^{m'} = \frac{1}{2}\epsilon^{m'n'o'p'} u_{n'} F_{o'p'}. \quad \text{(A2)}$$

From this definition, it follows that $B^{m'} = b^{m'}$ in the fluid frame. The equivalent four-vector in the Boyer–Lindquist Frame is then

$$b^{\mu} = e^{\mu}{}_{(m)} \Lambda^{(m)}{}_{(n')} b^{(n')}, \quad \text{(A3)}$$

where $\Lambda^{(m)}{}_{(n')} = (\Lambda^{(n')}{}_{(m)})^{-1}$ is the inverse Lorentz transformation. The components of b^{μ} are

$$b^t = \beta\gamma\sqrt{\frac{\Xi}{\Delta\Sigma}}(\sin(\theta)\sin(\iota)\cos(\eta - \phi) + \cos(\theta)\cos(\iota)) \quad \text{(A4a)}$$

$$b^r = \sqrt{\frac{\Delta}{\Sigma}}\left(\frac{1}{8}\sin(\iota)(2(\gamma + 3)\cos(\eta) - (\gamma - 1)(-4\sin^2(\theta) \times \cos(\eta - 2\phi) + \cos(\eta - 2\theta) + \cos(\eta + 2\theta))\right) + (\gamma - 1)\sin(\theta)\cos(\theta)\cos(\iota)\cos(\phi)) \quad \text{(A4b)}$$

$$b^{\theta} = -\frac{(\gamma - 1)\sin(2\theta)\sin(\iota)\cos(\eta - \phi) + \cos(\iota)((\gamma - 1)\cos(2\theta) + \gamma + 1)}{2\sqrt{\Sigma}} \quad \text{(A4c)}$$

$$b^{\phi} = \beta\gamma\omega\sqrt{\frac{\Xi}{\Delta\Sigma}}(\sin(\theta)\sin(\iota)\cos(\eta - \phi) + \cos(\theta)\cos(\iota)) + \frac{1}{8}\csc(\theta)\sqrt{\frac{\Sigma}{\Xi}}(\sin(\eta)\sin(\iota)(\gamma\cos(2(\theta + \phi)) + (\gamma - 1)\cos(2(\theta - \phi)) - 2 \times (\gamma - 1)\cos(2\theta) - 2\gamma\cos(2\phi) + 2\gamma - \cos(2(\theta + \phi)) + 2\cos(2\phi) + 6) + 8(\gamma - 1) \times \sin(\theta)\sin(\phi)(\cos(\eta)\sin(\theta)\sin(\iota) \times \cos(\phi) + \cos(\theta)\cos(\iota))). \quad \text{(A4d)}$$

A.3. Image Indexing

The Kerr spacetime naturally gives rise to strong-lensing effects where an object will produce infinitely many images when seen by a distant observer (see, e.g., Cunningham & Bardeen 1973; Ohanian 1987). A prescription for indexing the infinity of images formed from a single object is then useful when modeling observables. Previous works have focused

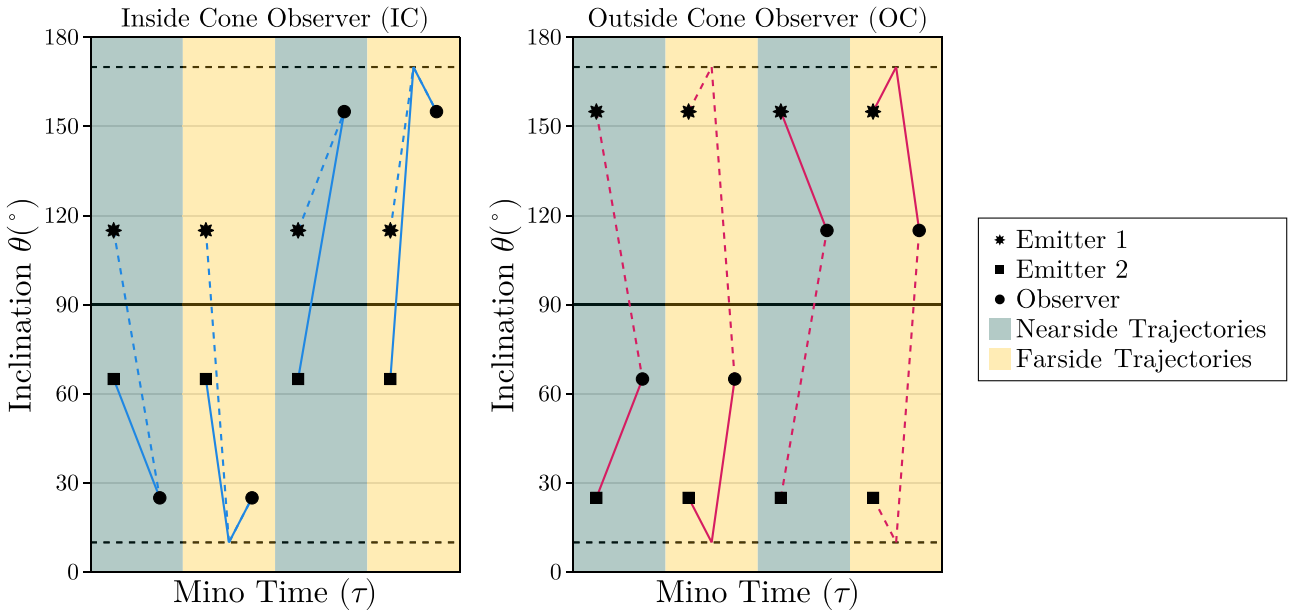

Figure 14. Schematic diagram showing the types of trajectories that can make up the $n = 0$ subimage. Multiple configurations are shown. The labels emitter $1/2$ indicate cases for which the emitter is above/below the equatorial plane. The left panel shows the trajectories for observer and emitter configurations where the observer is inside the cone (IC), while the right panel shows configuration for where the observer is outside the cone (OC). The green highlighted trajectories originate from emitters that are on the side of the cone near to the observer, while those highlighted in orange originate from the side far from the observer. The black solid line highlights the equatorial plane, and is the reference line from where the antiderivative used to evaluate the integral Equation (A9) is defined. The dashed lines indicate the location of the turning points in θ, which bounds the photon trajectories.

on schemes that index images based on the number of equatorial crossings, or number of turning points accrued in θ in a photon trajectory (see, e.g., Gralla & Lupsasca 2020; Johnson et al. 2020), but such definitions are ambiguous for general emitter–observer configurations. In particular, we show classes of trajectories associated with various emitter and observer configurations in Figure 14 for $n = 0$ emission as determined by affine length ordering. An analysis of this figure indicates that the affine length ordered $n = 0$ images of each trajectory could result in a different indexing when using either the equatorial crossing or the turning point definitions. In particular, this figure indicates that the two definitions are not equivalent, and that there exists emitter and observer configurations, which do not have $n = 0$ images in either the equatorial crossing or turning point indexing definitions. Here, we define a generic strategy for indexing null-geodesic trajectories in the Kerr spacetime.

An observer at infinity sets up a screen with coordinates

$$\alpha = -\frac{p^{\phi}}{p^{r}} = -\frac{\lambda}{\sin\theta_{\rm o}} \tag{A5}$$

$$\beta = -\frac{p^{\theta}}{p^{r}} = -\sqrt{\Theta(\theta_{\rm o}, \lambda, \eta)}\,, \tag{A6}$$

where

$$\Theta(\theta) = \sqrt{\eta + a^2\cos^2\theta - \lambda^2\cot^2\theta} \tag{A7}$$

is the angular potential of a null-geodesic. Every pixel on the screen of an asymptotic observer can be associated with a unique null ray of the Kerr exterior. This fact allows for a local indexing scheme, which orders images on pixels by the total affine parameter or the Mino time of the trajectories that generated them. We note that a indexing scheme based on Mino time is equivalent to one performed on affine time since the two are related through the relationship

$$d\tau = \frac{d\lambda}{\Sigma}, \tag{A8}$$

where $\Sigma \geqslant 0$.

We define the Mino time for an nth indexed trajectory, which connects a pixel to a bulk location. We note that the Mino time can be expressed in terms of quadratures of θ as

$$\Delta\tau = \int_{\theta_s}^{\theta_{\rm o}} \frac{\Sigma}{\pm p_{\theta}(\theta)} d\theta = \int_{\theta_s}^{\theta_{\rm o}} \pm\frac{d\theta}{\sqrt{\Theta(\theta)}}, \tag{A9}$$

where

$$\frac{d\theta}{\sqrt{\Theta}} = \frac{d\theta}{\sqrt{\eta + a^2\cos^2\theta - \lambda^2\cot^2\theta}} \tag{A10}$$

$$= \frac{1}{2}\frac{du}{\sqrt{u}\sqrt{\eta - (\eta + \lambda^2 - a^2)u + a^2u^2}}, \tag{A11}$$

with $u = \cos^2\theta$, and θ_s and $\theta_{\rm o}$ being the emission and observation Boyer–Lindquist inclination of the photon. The symbol $\int$ of Equation (A9) indicates a path integral.

Any trajectory of Equation (A9) can be classified as "Ordinary" or "Vortical." The classification is based off the fact that any point along the photon's trajectory must satisfy the constraint, $\Theta(\theta) \geqslant 0$, which implies that the rays have turning points at

$$u_{\pm} = \triangle_{\theta} \pm \sqrt{\triangle_{\theta}^2 + \frac{\eta}{a^2}}, \quad \triangle_{\theta} = \frac{1}{2}\left(1 - \frac{\eta + \lambda^2}{a^2}\right). \tag{A12}$$

The classification of trajectories into "Ordinary" or "Vortical" then follows from the nature of the roots (see Gralla & Lupsasca 2020), where geodesics that are said to undergo

"Ordinary" motion satisfy

$$\arccos(\sqrt{u_+}) < \theta < \arccos(-\sqrt{u_+}), \tag{A13}$$

while those that undergo "Vortical Motion" satisfy

$$\begin{aligned}&\arccos(-\sqrt{u_-}) < \theta < \arccos(-\sqrt{u_+})\\ &\text{or}\quad \arccos(\sqrt{u_+}) < \theta < \arccos(\sqrt{u_-}).\end{aligned} \tag{A14}$$

Our goal of this section is related to the length of the trajectory of a photon to an index, n, that labels the subimage, which the photon generates. To aid in this analysis, we define the integrals,

$$G_{\theta_s} = \frac{1}{2}\int_0^{\cos(\theta_s)} \frac{du}{\sqrt{u}\sqrt{\eta - (\eta + \lambda^2 - a^2)u + a^2u^2}}, \tag{A15}$$

$$G_{\theta_o} = \frac{1}{2}\int_0^{\cos(\theta_o)} \frac{du}{\sqrt{u}\sqrt{\eta - (\eta + \lambda^2 - a^2)u + a^2u^2}}, \tag{A16}$$

$$\hat{G}_\theta = 2\begin{cases}\displaystyle\int_{\arccos(\sqrt{u_+})}^{\arccos(-\sqrt{u_+})} \frac{du}{\sqrt{u}\sqrt{\eta - (\eta + \lambda^2 - a^2)u + a^2u^2}}, & \text{Ordinary}\\ \displaystyle\int_{\arccos(\mp\sqrt{u_-})}^{\arccos(-\sqrt{u_+})} \frac{du}{\sqrt{u}\sqrt{\eta - (\eta + \lambda^2 - a^2)u + a^2u^2}}, & \text{Vortical}\end{cases}. \tag{A17}$$

These will be useful since the total Mino time can be written as linear combination of these functions. In general, the total Mino time of the nth image is

$$\Delta\tau_n = n\hat{G}_\theta + \Delta\tau_0, \tag{A18}$$

which is dependent on the emission and observation inclinations, as well as the pixel on the observer's screen that the photon lands on.

Refining Equation (A18) into a definition requires specifying the Mino time of the zeroth image, $\Delta\tau_0$. Our approach is to define $\Delta\tau_0$ from the observational properties of a curve $\gamma_\phi = (t, r(\phi), \theta_s, \phi)$, which is taken to be closed in bulk space. γ_ϕ will thus result in an image of a closed curve on the observer's screen that will either be intersected by the $\beta = 0$ axis, or lie entirely to one side of it. We use the fact that γ_ϕ can be thought of as the intersection of a rigid cone and a rigid 2D surface, to define the situation where the image of γ_ϕ intersects $\beta = 0$ as the case where the observer is positioned "inside the cone" (IC), while the other case will be for an observer positioned "outside the cone" (OC). We have chosen this classification to be consistent with that of Papoutsis et al. (2023), and will quantify it through the definition of a variable,

$$\text{isincone} = \begin{cases}\text{true}, & |\cos\theta_o| > |\cos\theta_s|, \text{ inside the cone (IC)}\\ \text{false}, & |\cos\theta_o| < |\cos\theta_s|, \text{ outside the cone (OC)}\end{cases}. \tag{A19}$$

One observational distinction that can be made about γ_ϕ is whether it originated from the "farside" of the cone, or the "nearside" with respect to the observer. This distinction allows us to define $\Delta\tau_0$ in the following way for IC observers as

$$\Delta\tau_0|_{\text{IC}} = \begin{cases} G_o + (-1)^{\nu_{\text{indir}}} G_s & \text{nearside},\\ \hat{G} - G_o + (-1)^{\nu_{\text{indir}}} G_s & \text{farside},\end{cases} \tag{A20}$$

where

$$\nu_{\text{indir}} = \frac{1}{2}(\text{sign}[\cos(\theta_o)] + \text{sign}[\cos(\theta_s)]). \tag{A21}$$

An implication of Equation (A6) is that $\text{sign}(\beta) = \text{sign}(p_\theta)|_{r=\infty}$ of a photon received by an asymptotic observer. We will use this fact to classify trajectories seen by IC observers as either having originated from the "farside" or "nearside" through the label

$$\text{isfarside} = (\text{sign}(\beta) > 0) \veebar (\cos\theta_o < 0). \tag{A22}$$

We can define $\Delta\tau|_{\text{OC}}$ in a similar way to $\Delta\tau|_{\text{IC}}$. The labeling of emission as farside versus nearside is however implicit since image (γ_ϕ) lies to one side of theta $\beta = 0$, and thus will depend on $\text{sign}(p_\theta)|_{r=r_s}$. We therefore define $\Delta|_{\text{OC}}$ as

$$\Delta\tau_0|_{\text{OC}} = \begin{cases} G_s + (-1)^{\nu_{\text{indir}}} G_o & \text{nearside},\\ \hat{G} - G_s + (-1)^{\nu_{\text{indir}}} G_o & \text{farside},\end{cases} \tag{A23}$$

whose form we would like to emphasize is similar to $\Delta\tau_0|_{\text{IC}}$, but with G_s and G_o swapped. Thus, we have that

$$\Delta\tau_0 = \begin{cases}\Delta\tau_0|_{\text{IC}} & |\cos\theta_o| > |\cos\theta_s|,\\ \Delta\tau_0|_{\text{OC}} & |\cos\theta_o| < |\cos\theta_s|.\end{cases} \tag{A24}$$

Figure 14 shows a summary of the classification of $\Delta\tau_0$ trajectories.

Equation (A24) can be further simplified with Boolean algebra. We define the ν_θ at the points of emission as

$$\nu_\theta = \text{sign}(p_\theta(\theta_s)) = \begin{cases}(-1)^{n+\text{sign}(\theta_o - \theta_s)+1} & \text{IC},\\ (-1)^{\text{sign}\left(\frac{\pi}{2} - \theta_s\right)+1} & \text{near side \& OC},\\ (-1)^{\text{sign}\left(\theta_s - \frac{\pi}{2}\right)+1} & \text{far side \& OC},\end{cases} \tag{A25}$$

which allows the total Mino time accrued to be written as

$$\Delta\tau_n = \begin{cases} n\hat{G} - \text{sign}(\beta)G_o + \nu_\theta G_s & \text{nearside},\\ (n+1)\hat{G} - \text{sign}(\beta)G_o + \nu_\theta G_s & \text{farside},\end{cases} \tag{A26}$$

where n is the image index.

Appendix B
Image Domain

Section 3 discusses the details of our image-domain study of our semianalytic models. The images analyzed were used to illustrate our models' capabilities for reproducing structures seen in various time-averaged GRMHD simulations, MAD and SANE. We also study the robustness of our model at producing representative images of GRMHD at various inclinations and at limited resolution. We show that the parameters that define the representative images are, in general, consistent with the parameters of the true GRMHD simulations. Table 4 lists a summary of the parameters that we used to define our models, along with the parameters that were fitted from GRMHD with our combination model in Figure 3. The GRMHD model used in Figure 3 was of a retrograde MAD GRMHD. We note that the representative models at 30° and 50° are also described by a retrograde accretion flow (the accretion flow is retrograde if the signs of χ and a differ in our convention). We also show additional images of fits to 0.5 spin MAD and SANE GRMHD simulations in Figure 15, where we find similar results as in Figure 2. All fits shown in Section 3 were to high spin images of GRMHD.

Table 4
Summary of Results from the NxCORR Fit Study of Figure 3

Param.	Description	Units	Range	Best-fit Param.			
				30°	50°	70°	90°
θ_g	Mass-to-distance ratio	μas	[1.5, 8]	5.04	5.04	5.04	4.99
a	Black hole dimensionless spin	…	[−1, 0]	−0.96	−0.95	−0.95	−0.89
θ_o	Observer inclination	deg	$[\theta_t - 20, \theta_t + 20]$	27	45	55	70
θ_s	Cone opening angle	deg	[20, 90]	67	70	61	77
p.a.	Position angle of projected spin axis	deg	…	…	…	…	…
$R_{\rm cone}$	Characteristic radius of emission on conical component	$\frac{GM}{c^2}$	[1, 10]	3.13	4.36	5.26	4.27
$p_{1\rm cone}$	Inner exponent of the cone intensity profile	…	[0.1, 10]	0.79	0.27	0.15	0.43
$p_{2\rm cone}$	Outer exponent of the cone intensity profile	…	[1, 10]	3.28	3.57	3.94	5.56
$\chi_{\rm cone}$	Fluid velocity azimuthal angle in ZAMO frame	deg	[−180, 180]	180	180	100	105
$\iota_{\rm cone}$	Orthogonal angle of magnetic field conical component	deg	[0, 90]	64	90	65	88
$\beta_{v\rm cone}$	Fluid speed of conical component in ZAMO frame	c	[0, 0.9]	0.38	0.18	0.10	0.16
$\sigma_{\rm cone}$	Spectral index of conical component	…	[−1, 3]	−0.01	−0.19	1.14	2.37
$\eta_{\rm cone}$	Tangential angle of magnetic field conical component	deg	[−180, 180]	162	10	175	−7
$R_{\rm disk}$	Characteristic radius of emission on equatorial component	$\frac{GM}{c^2}$	[1, 10]	5.36	5.67	4.45	1.01
$p_{1\rm disk}$	Inner exponent of the disk intensity profile	…	[0.1, 10]	0.10	0.1	0.10	9.43
$p_{2\rm disk}$	Outer exponent of the disk intensity profile	…	[1, 10]	4.47	7.12	5.63	1.55
$\chi_{\rm disk}$	Fluid velocity azimuthal angle in ZAMO frame	deg	[−180, 180]	84	79	129	148
$\iota_{\rm disk}$	Orthogonal angle of magnetic field equatorial component	deg	[0, 90]	79	90	80	82
$\beta_{v\rm disk}$	Fluid speed of equatorial component in ZAMO frame	c	[0, 0.9]	0.17	0.41	0.19	0.09
$\sigma_{\rm disk}$	Spectral index of equatorial component	…	[−1, 3]	1.98	3.00	1.78	−1.11
η_{disk}	Tangential angle of magnetic field equatorial component	deg	[−180, 180]	10	−19	180	90
r_J	Relative flux component between cone and disk	…	[0, 1]	0.5	0.48	0.81	0.58

Note. The parameters and the search ranges shown include all the parameters that were used in the image-domain study of Section 3 across all model types. θ_t in the above table refers to the true spin inclination that our model was fitted to. There are no entries for the p.a. under the "Best-fit Parameters" column since it was fixed to the true value during the fits.

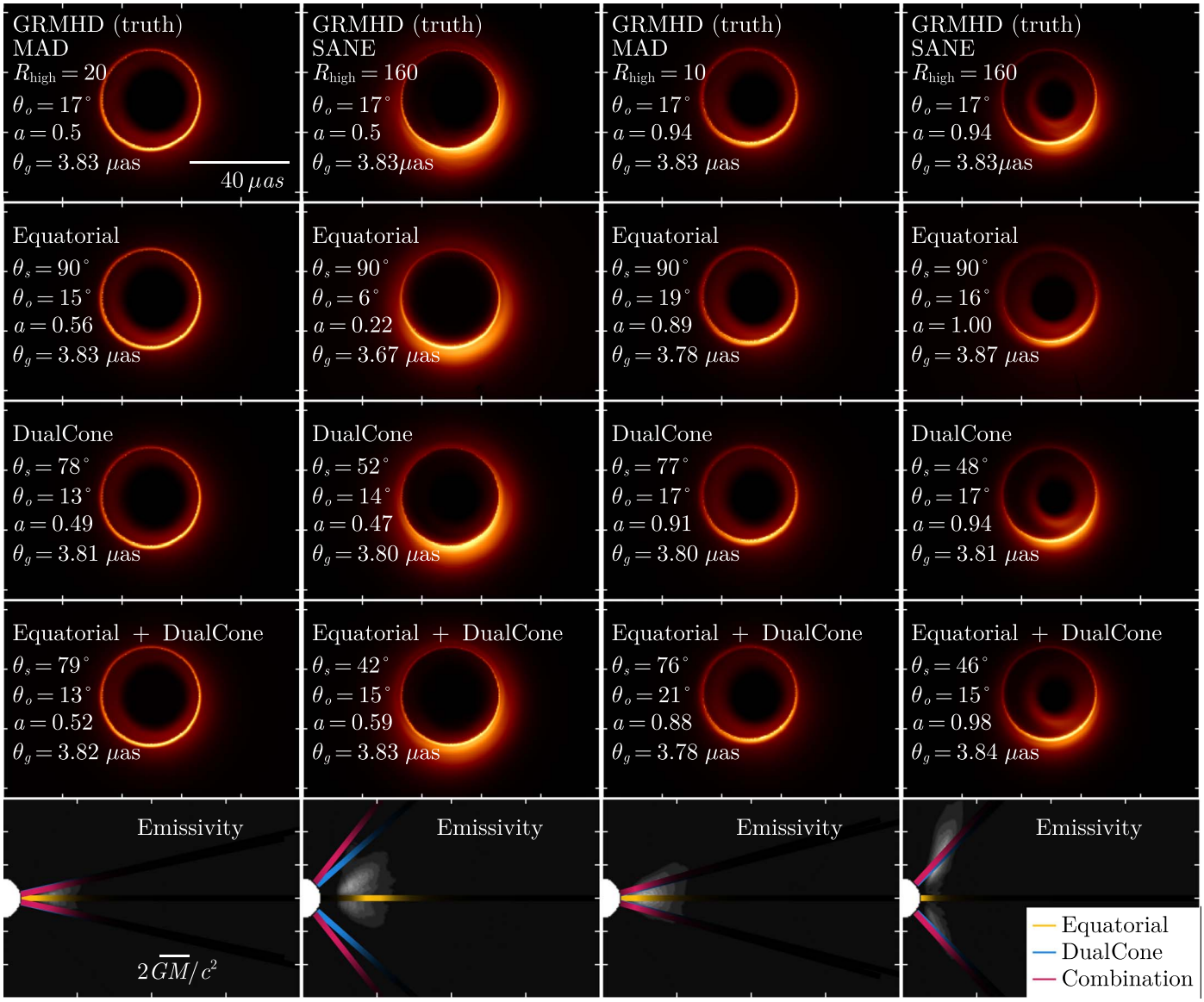

Figure 15. Best-fit (by optimizing the normalized cross correlation; see Section 3) equatorial, dual-cone, and combination (equatorial + dual-cone) models to four GRMHD simulations of M87*. The four models are (left) $a = 0.5$, $R_{\rm high} = 20$, MAD, (center-left) $a = 0.5$, $R_{\rm high} = 160$, SANE, (center-right) $a = 0.94$, $R_{\rm high} = 10$, MAD, and (right) $a = 0.94$, $R_{\rm high} = 160$, SANE. The bottom row compares the model emissivity to the GRMHD emissivity. The equatorial model shows the most significant errors in the best-fit parameters. For the dual-cone model, the mass-to-distance ratio of the best-fit model is accurate to within ∼1%, the spin is accurate to within 6%, and the inclination is accurate to within 4° for each of the four GRMHD simulations.

Appendix C
Visibility Domain

Here, we show the full corner plots for the visibility-domain fits of Section 4. These include the corner plots for the self-fit (Figure 16), the GRMHD fit (Figure 17), and the 2017 M87* data fit (Figure 18).

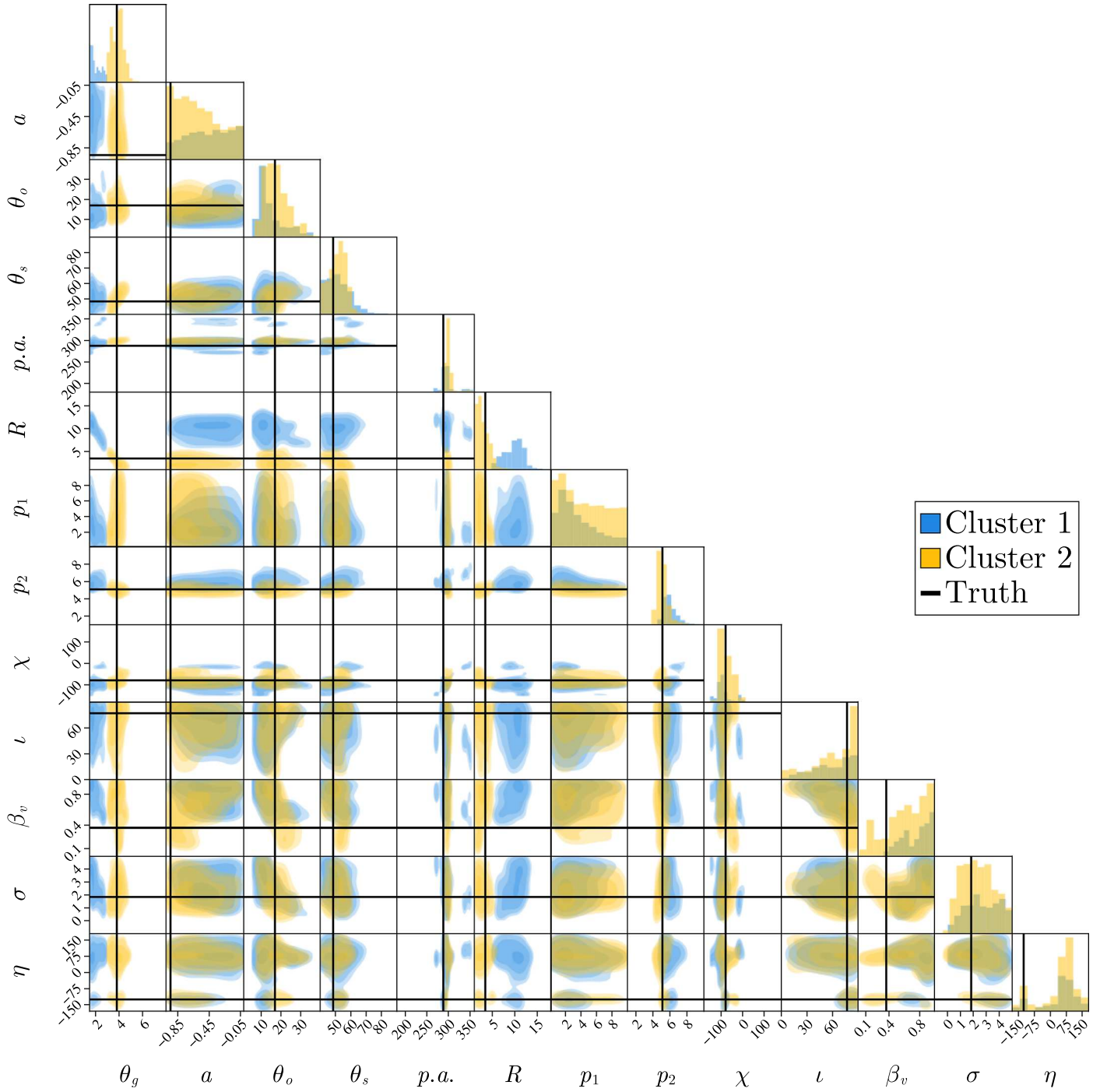

Figure 16. Full triangle plot for dual-cone model fits to synthetic data generated from a dual-cone model (see Section 4.5 for details).

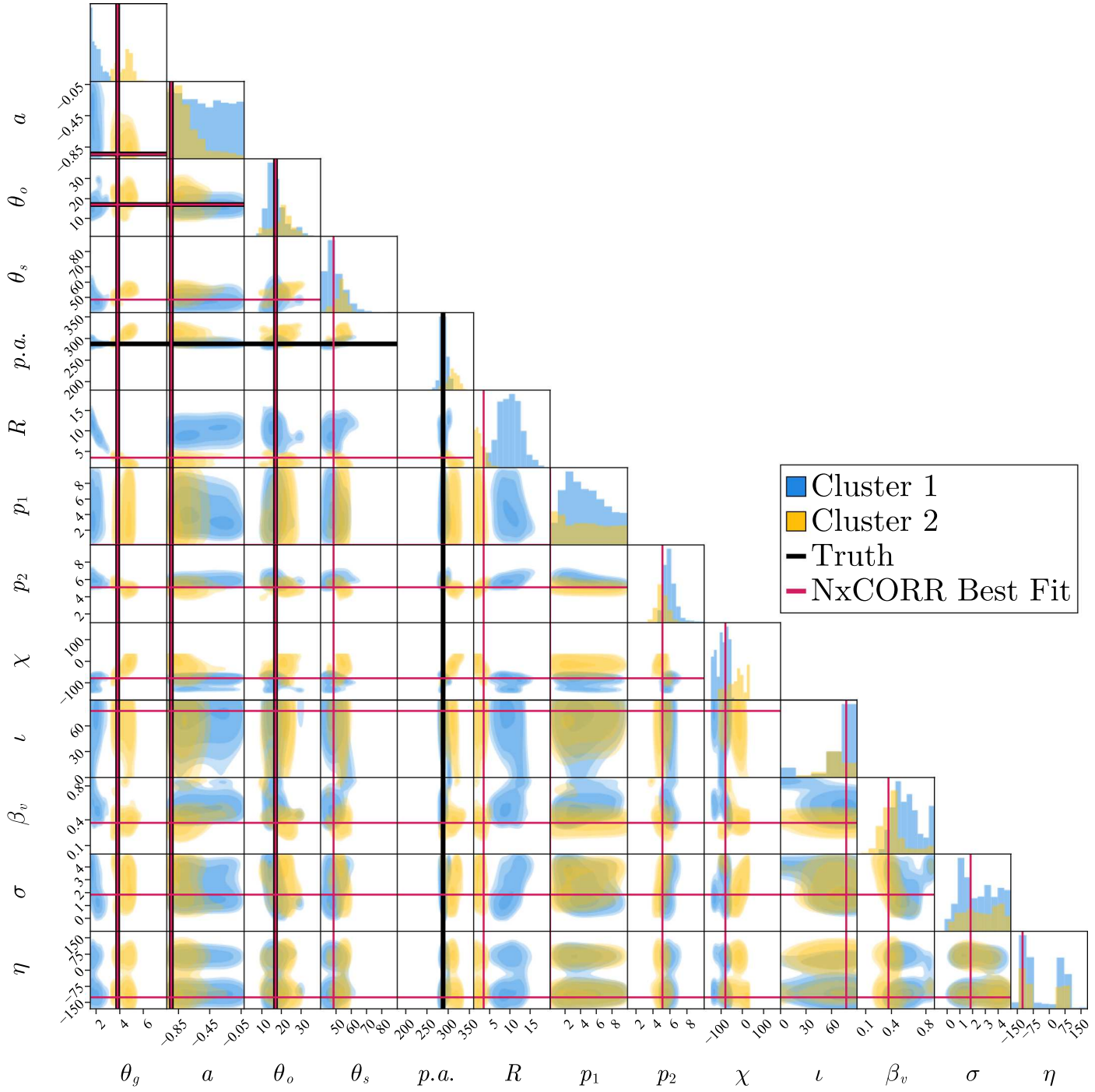

Figure 17. Full triangle plot for dual-cone model fits to synthetic data generated from a prograde $R_{\rm high} = 160$ SANE simulation of M87* (see Section 4.6 for details).

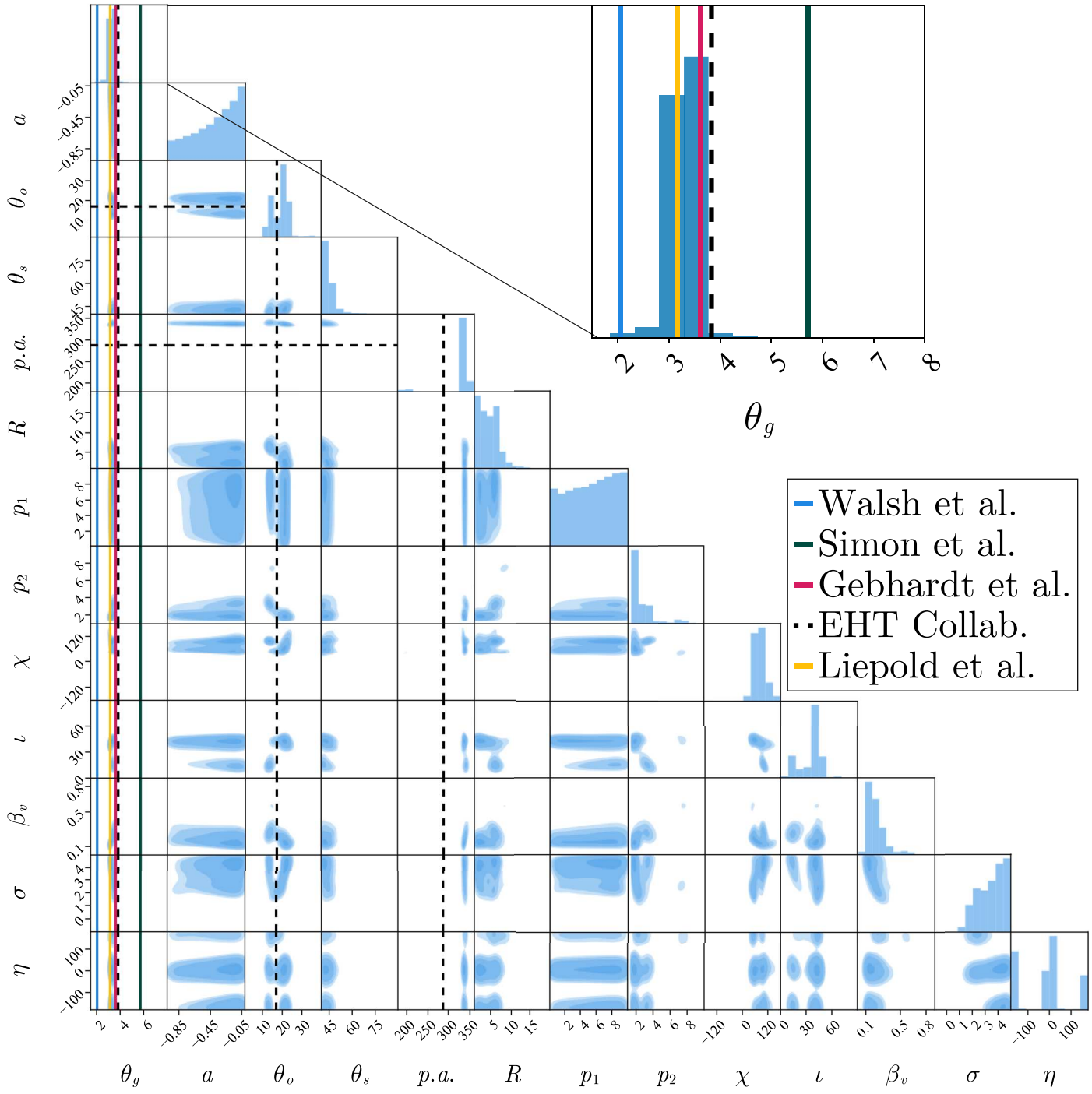

Figure 18. Full triangle plot for dual-cone model fits to EHT measurements of M87* (see Section 4.7 for details).

ORCID iDs

Dominic O. Chang https://orcid.org/0000-0001-9939-5257
Michael D. Johnson https://orcid.org/0000-0002-4120-3029
Paul Tiede https://orcid.org/0000-0003-3826-5648
Daniel C. M. Palumbo https://orcid.org/0000-0002-7179-3816

References

Bao, G., Hadrava, P., & Ostgaard, E. 1994, ApJ, 435, 55
Bardeen, C. T., & Cunningham, J. M. 1973, ApJ, 183, 237
Bardeen, J. M., & Petterson, J. A. 1975, ApJL, 195, L65
Bardeen, J. M., Press, W. H., & Teukolsky, S. A. 1972, ApJ, 178, 347
Bezanson, J., Edelman, A., Karpinski, S., & Shah, V. B. 2017, SIAMR, 59, 65
Blackburn, L., Pesce, D. W., Johnson, M. D., et al. 2020, ApJ, 894, 31
Blandford, R., Meier, D., & Readhead, A. 2019, ARA&A, 57, 467
Boerner, T. J., Deems, S., Furlani, T. R., Knuth, S. L., & Towns, J. 2023, Practice and Experience in Advanced Research Computing, PEARC '23 (ACM), 173
Broderick, A. E., Fish, V. L., Doeleman, S. S., & Loeb, A. 2009, ApJ, 697, 45
Broderick, A. E., Fish, V. L., Doeleman, S. S., & Loeb, A. 2011, ApJ, 735, 110
Broderick, A. E., Fish, V. L., Johnson, M. D., et al. 2016, ApJ, 820, 137
Broderick, A. E., Gold, R., Karami, M., et al. 2020, ApJ, 897, 139
Broderick, A. E., Johannsen, T., Loeb, A., & Psaltis, D. 2014, ApJ, 784, 7
Broderick, A. E., & Loeb, A. 2009, ApJ, 697, 1164
Bronzwaer, T., Davelaar, J., Younsi, Z., et al. 2018, A&A, 613, A2
Carter, B. 1968, PhRv, 174, 1559

Chael, A., Johnson, M. D., & Lupsasca, A. 2021, ApJ, 918, 6
Chael, A., Lupsasca, A., Wong, G. N., & Quataert, E. 2023, ApJ, 958, 65
Chael, A. A., Johnson, M. D., Bouman, K. L., et al. 2018, ApJ, 857, 23
Chandrasekhar, S. 1984, The Mathematical Theory of Black Holes (Dordrecht: Springer), 5
Chang, D., 2024 Bayesian Black Hole Photogrammetry, v1.0, Zenodo, doi:10.5281/zenodo.13161578
Chatterjee, K., Younsi, Z., Liska, M., et al. 2020, MNRAS, 499, 362
Cui, Y., Hada, K., Kawashima, T., et al. 2023, Natur, 621, 711
Cunningham, C. T., & Bardeen, J. M. 1973, ApJ, 183, 237
Dexter, J., & Agol, E. 2009, ApJ, 696, 1616
Dexter, J., McKinney, J. C., & Agol, E. 2012, MNRAS, 421, 1517
Duschl, W. J. 1999, RvMA, 12, 221
EHTC, Akiyama, K., Alberdi, A., et al. 2019a, ApJL, 875, L4
EHTC, Akiyama, K., Alberdi, A., et al. 2019b, ApJL, 875, L6
EHTC, Akiyama, K., Alberdi, A., et al. 2019c, ApJL, 875, L1
EHTC, Akiyama, K., Alberdi, A., et al. 2019d, ApJL, 875, L2
EHTC, Akiyama, K., Alberdi, A., et al. 2019e, ApJL, 875, L3
EHTC, Akiyama, K., Alberdi, A., et al. 2019f, ApJL, 875, L5
EHTC, Akiyama, K., Alberdi, A., et al. 2022a, ApJL, 930, L12
EHTC, Akiyama, K., Alberdi, A., et al. 2022b, ApJL, 930, L13
EHTC, Akiyama, K., Alberdi, A., et al. 2022c, ApJL, 930, L14
EHTC, Akiyama, K., Alberdi, A., et al. 2022d, ApJL, 930, L15
EHTC, Akiyama, K., Alberdi, A., et al. 2022e, ApJL, 930, L16
EHTC, Akiyama, K., Alberdi, A., et al. 2022f, ApJL, 930, L17
EHTC, Akiyama, K., Alberdi, A., et al. 2023, ApJL, 957, L20
EHTC, Akiyama, K., Alberdi, A., et al. 2024a, ApJL, 964, L25
EHTC, Akiyama, K., Alberdi, A., et al. 2024b, ApJL, 964, L26
EHTC, Akiyama, K., Alberdi, A., et al. 2024c, A&A, 681, A79
EHTC, Akiyama, K., Algaba, J. C., et al. 2021a, ApJL, 910, L12
EHTC, Akiyama, K., Algaba, J. C., et al. 2021b, ApJL, 910, L13
Emami, R., Ricarte, A., Wong, G. N., et al. 2023, ApJ, 950, 38
Falcke, H., Goss, W. M., Matsuo, H., et al. 1998, ApJ, 499, 731
Galishnikova, A., Philippov, A., & Quataert, E. 2023, ApJ, 957, 103
Gammie, C. F., McKinney, J. C., & Tóth, G. 2003, ApJ, 589, 444
Gates, D. E. A., Hadar, S., & Lupsasca, A. 2021, PhRvD, 103, 044050
Gebhardt, K., Adams, J., Richstone, D., et al. 2011, ApJ, 729, 119
Gelles, Z., Himwich, E., Johnson, M. D., & Palumbo, D. C. M. 2021, PhRvD, 104, 044060
Gralla, S. E., Holz, D. E., & Wald, R. M. 2019, PhRvD, 100, 024018
Gralla, S. E., & Lupsasca, A. 2020, PhRvD, 101, 044032
Himwich, E., Johnson, M. D., Lupsasca, A., & Strominger, A. 2020, PhRvD, 101, 084020
Jeter, B., & Broderick, A. E. 2021, ApJ, 908, 139
Johnson, M. D., Lupsasca, A., Strominger, A., et al. 2020, SciA, 6, eaaz1310
Liepold, E. R., Ma, C.-P., & Walsh, J. L. 2023, ApJL, 945, L35
Liska, M., Tchekhovskoy, A., Ingram, A., & van der Klis, M. 2019, MNRAS, 487, 550
Lockhart, W., & Gralla, S. E. 2022, MNRAS, 517, 2462
Macchetto, F., Marconi, A., Axon, D. J., et al. 1997, ApJ, 489, 579
Medeiros, L., Psaltis, D., Lauer, T. R., & Özel, F. 2023, ApJ, 943, 144
Mertens, F., Lobanov, A. P., Walker, R. C., & Hardee, P. E. 2016, A&A, 595, A54
Mino, Y. 2003, PhRvD, 67, 084027
Mościbrodzka, M., Falcke, H., & Shiokawa, H. 2016, A&A, 586, A38
Mościbrodzka, M., & Gammie, C. F. 2018, MNRAS, 475, 43
Narayan, R., Igumenshchev, I. V., & Abramowicz, M. A. 2003, PASJ, 55, L69
Narayan, R., Palumbo, D. C. M., Johnson, M. D., et al. 2021, ApJ, 912, 35
Narayan, R., Sadowski, A., Penna, R. F., & Kulkarni, A. K. 2012, MNRAS, 426, 3241
Neal, R. M. 2003, AnSta, 31, 705
Ohanian, H. C. 1987, AmJPh, 55, 428
Özel, F., Psaltis, D., & Younsi, Z. 2022, ApJ, 941, 88
Palumbo, D. C. M., Gelles, Z., Tiede, P., et al. 2022, ApJ, 939, 107
Palumbo, D. C. M., & Wong, G. N. 2022, ApJ, 929, 49
Palumbo, D. C. M., Wong, G. N., & Prather, B. S. 2020, ApJ, 894, 156
Papoutsis, E., Bauböck, M., Chang, D., & Gammie, C. F. 2023, ApJ, 944, 55
Prather, B., Wong, G., Dhruv, V., et al. 2021, JOSS, 6, 3336
Prieto, M. A., Fernández-Ontiveros, J. A., Markoff, S., Espada, D., & González-Martín, O. 2016, MNRAS, 457, 3801
Pu, H.-Y., Akiyama, K., & Asada, K. 2016, ApJ, 831, 4
Pu, H.-Y., & Broderick, A. E. 2018, ApJ, 863, 148
Rauch, K. P., & Blandford, R. D. 1994, ApJ, 421, 46
Simon, D. A., Cappellari, M., & Hartke, J. 2023, MNRAS, 527, 2341
Surjanovic, N., Biron-Lattes, M., Tiede, P., et al. 2023, arXiv:2308.09769
Syed, S., Bouchard-Côté, A., Deligiannidis, G., & Doucet, A. 2021, Journal of the Royal Statistical Society Series B: Statistical Methodology, 84, 321
Takahashi, R. 2004, ApJ, 611, 996
Thompson, A. R., Moran, J. M., & Swenson, G. W. 2017, Interferometry and Synthesis in Radio Astronomy (Cham: Springer)
Thorne, K. S., Price, R. H., & MacDonald, D.A. 1986, Black Holes (New Haven, CT: Yale Univ. Press)
Thyagarajan, N., Nityananda, R., & Samuel, J. 2022, PhRvD, 105, 043019
Tiede, P. 2022, JOSS, 7, 4457
Tiede, P., Broderick, A. E., & Palumbo, D. C. M. 2022, ApJ, 925, 122
Walker, M., & Penrose, R. 1970, CMaPh, 18, 265
Walker, R. C., Hardee, P. E., Davies, F. B., Ly, C., & Junor, W. 2018, ApJ, 855, 128
Walsh, J. L., Barth, A. J., Ho, L. C., & Sarzi, M. 2013, ApJ, 770, 86
Wong, G. N., Du, Y., Prather, B. S., & Gammie, C. F. 2021, ApJ, 914, 55
Wong, G. N., Prather, B. S., Dhruv, V., et al. 2022, ApJS, 259, 64
Younsi, Z., Psaltis, D., & Özel, F. 2023a, ApJ, 942, 47
Yuan, F., & Narayan, R. 2014, ARA&A, 52, 529